

Biofunctionalized Graphene Quantum Dots Based Fluorescent Biosensor toward Efficient Detection of Small Cell Lung Cancer

Ashish Kalkal,¹ Rangadhar Pradhan,¹ Sachin Kadian, Gaurav Manik, and Gopinath Packirisamy*



Cite This: *ACS Appl. Bio Mater.* 2020, 3, 4922–4932



Read Online

ACCESS |



Metrics & More



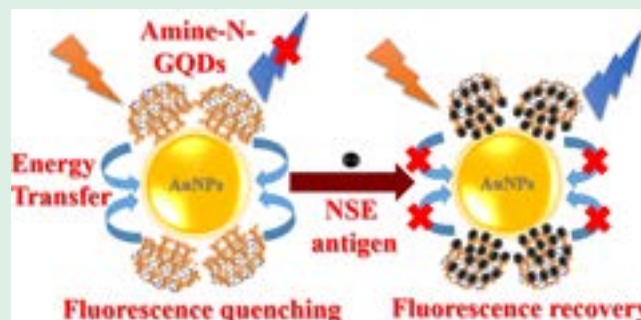
Article Recommendations



Supporting Information

ABSTRACT: Quantitative detection of cancer biomarkers with higher accuracy and sensitivity provides an effective platform for screening, monitoring, early diagnosis, and disease surveillance. The present work demonstrates the fabrication and application of fluorescent turn-on biosensor for ultrasensitive detection of small cell lung cancer biomarker utilizing biofunctionalized graphene quantum dots as the energy donor and gold nanoparticles (AuNPs) as the energy acceptor. One-pot and the bottom-up hydrothermal route have been employed for the synthesis of *in situ* amine-functionalized and nitrogen-doped graphene quantum dots (amine-N-GQDs) and further characterized experimentally by different analytical techniques. The molecular simulation studies were performed using the Material Studio software for optimizing the possible chemical structure of synthesized amine-N-GQDs, a comprehensive analysis of experimental results to validate the presence of potential N-doping and amine functionalization sites. Then monoclonal neuron-specific enolase antibodies (anti-NSE) were covalently immobilized to amine-N-GQDs to provide the biofunctionalized GQDs (anti-NSE/amine-N-GQDs). A label-free and efficient fluorescent biosensor based on nanosurface energy transfer (NSET) between anti-NSE/amine-N-GQDs and AuNPs has been developed for neuron-specific enolase (NSE) detection. The fluorescence response studies of anti-NSE/amine-N-GQDs@AuNPs nanoprobe conducted as a function of NSE antigen exhibited fast response time (16 min), broader linear detection range (0.1 pg mL^{-1} to 1000 ng mL^{-1}), and remarkably low detection limit (0.09 pg mL^{-1}). Additionally, the fluorescent biosensor exhibited excellent performance in real samples, with an average recovery value of 94.69%.

KEYWORDS: biosensor, graphene quantum dots (GQDs), energy transfer, small cell lung cancer (SCLC), biomarker



1. INTRODUCTION

Lung cancer is known to be one of the most deadly forms of cancer, causing a large number of deaths worldwide. It can be classified into two major dichotomies: small cell lung cancer (SCLC) and nonsmall cell lung cancer (NSCLC). SCLC is known for its tendency to metastasize early and rapid doubling time and is difficult to treat due to its initial high sensitivity to chemotherapy but invariable relapse and acquired chemo-resistance.¹ SCLC accounts for 15–20% of new lung cancer cases, and the majority of these cases are diagnosed at an advanced stage with serious illness.² Therefore, early diagnosis of SCLC is of utmost interest, providing increased chances for patient survival. In this context, the quantitative detection of elevated cancer biomarkers with higher accuracy and sensitivity provides an effective platform for screening, early diagnosis, and disease surveillance. Studies have reported that neuron-specific enolase (NSE) is a reliable, specific, and sensitive serum biomarker for the early diagnosis of SCLC and could assess the patient's recovery progress. In normal human beings, the serum NSE concentration has been recorded up to 12–13 ng mL^{-1} , whereas in SCLC patients, serum NSE concentration

is found to be more than 35 ng mL^{-1} .³ For the SCLC diagnosis, a cutoff value of 16–25 ng mL^{-1} has been reported.¹ Therefore, it is highly desirable to develop an efficient, selective, inexpensive, and sensitive diagnostic tool that can provide early and accurate NSE detection and can be used for continuous assessment.

Recently, nonradiative energy transfer (ET) based fluorescent sensors have drawn tremendous research interest in detecting the biomolecular interactions, measuring nanoscaled information in clinical applications and medical fields.^{4–9} These sensors provide various advantages like rapid, reliable, and highly sensitive response with minimum background noise, easy operation, high specificity, the requirement of simple instrumentation, and capability for real-time detection.^{4,10,11} It

Received: April 17, 2020

Accepted: June 9, 2020

Published: June 9, 2020



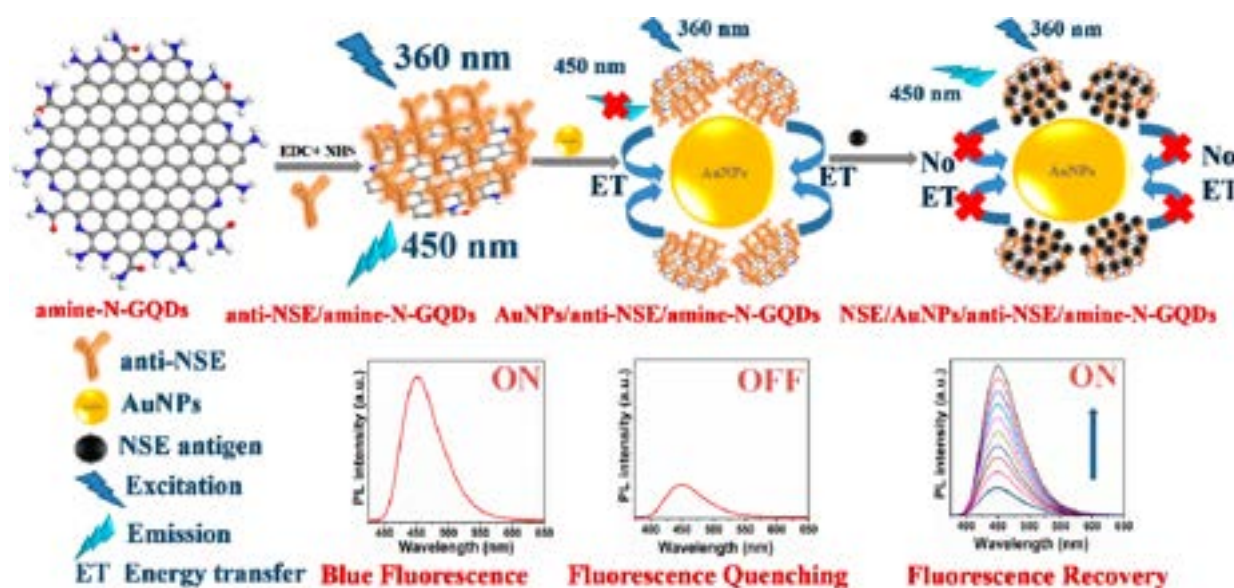


Figure 1. Pictorial representation indicating the mechanism of the fluorescent biosensor for small cell lung cancer biomarker detection.

has been reported that for enhancing the efficiency and performance of energy transfer based fluorescent biosensors, the selection of appropriate donor–acceptor pair is crucial.^{12,13} In traditional Förster resonance energy transfer (FRET) based sensors, organic dyes have been widely used as energy donor–acceptor pair. However, photobleaching, small Stokes shift, narrow excitation band, long-term cytotoxic effects, and the presence of toxic precursors are the reported challenges of these materials.¹⁴ Moreover, it has been reported that conventional FRET sensors have a limited detectable distance of ~ 6 nm wherein ET efficiency follows $1/d^6$ distance (between donor–acceptor pair) dependence. Therefore, the exploration of nanomaterials based donor–acceptor pair with outstanding optical properties and excellent biocompatibility is highly demanded.^{15,16} In this context, gold nanoparticles (AuNPs) have emerged as a significant energy acceptor alternative to the organic dyes, following nanosurface energy transfer (NSET) mechanism. It has been reported that in the case of NSET, the energy can be transferred over a much longer distance (up to 50 nm) following $1/d^4$ distance dependence. Recently, Chen et al. reported and reviewed that NSET is the operational energy transfer mechanism in AuNPs for the quenching of fluorescent donors.^{17,18}

Similarly, carbon-based fluorescent nanomaterials, mainly graphene quantum dots (GQDs), have emerged as a promising alternative as energy donor due to their remarkable optical and electronic properties.^{19–24} Compared to semiconductor quantum dots (QDs) and organic dyes, GQDs exhibit good photostability, excellent biocompatibility, excellent water solubility, tunable size-dependent PL, broad excitation spectra, strong quantum confinement, and edge effects, making them a promising material as energy donor.^{19,20,25,26} However, low quantum yield (QY) and short fluorescence lifetime of GQDs restrict their practical biosensing applications.^{27,28} In recent years, a heteroatom doping or surface functionalization has been reported as a powerful means to improve the electronic and optical properties of GQDs.¹⁹ Doped GQDs have been reported with improved QY, long fluorescence lifetime, and other optical properties.^{29–31}

Furthermore, the surface functionalization with primary amine molecules convert the $-\text{COOH}$ and epoxy groups of GQDs to $-\text{CNHR}$ and $-\text{CONHR}$. These groups result in suppression of nonradiative electron–hole recombination and thereby enrich intrinsic state emission.¹⁹ Typically, compounds such as oylamine, oleic acid, 3-aminopropyltriethoxysilane (APTES), and 3-mercaptopropyltriethoxysilane (MPTES) have been widely utilized for *ex situ* surface functionalization.^{32,33} However, it has been reported that *ex situ* functionalization involves an extra step in the procedure to link the required functional group that may affect the fluorescence property and morphology of QDs.³⁴

Therefore, in this article, a one-pot and the bottom-up hydrothermal method has been used to obtain *in situ* amine-functionalized nitrogen-doped graphene quantum dots (amine-N-GQDs). The possible chemical structure of synthesized amine-N-GQDs has been optimized through the molecular simulation studies. Nitrogen doping and *in situ* amine functionalization have been validated using both theoretical and experimental characterization tools. Further, we have reported the biofunctionalized GQDs (anti-NSE/amine-N-GQDs) and AuNPs based fluorescent turn-on biosensor for ultrasensitive and quantitative NSE detection. The fluorescence response studies of fabricated biosensor conducted as a function of NSE antigen exhibited remarkable biosensing parameters in both standard and real samples.

2. EXPERIMENTAL SECTION

2.1. Synthesis of Amine-N-GQDs via Hydrothermal Method.

Low temperature, one-pot, and the bottom-up hydrothermal method have been utilized for the synthesis of amine-N-GQDs. Briefly, 2.1 g of citric acid was dispersed in 10 mL of distilled water under magnetic stirring. Next, 3.7 mL of diethylenetriamine (DETA) was added to the above solution and continued stirring to obtain a transparent solution. The resultant solution was transferred to a Teflon-lined hydrothermal pressure vessel. Afterward, the sealed hydrothermal vessel was placed in an electric oven and heated at 170 °C for the optimized duration of 5 h. After natural cooling to room temperature, the obtained solution was filtered using a 0.2 μm syringe filter to separate the large-sized particles. Further, the obtained solution was subjected to dialysis against water for 2 days (retained MWCF: 2 kDa) to remove remaining small molecules. Finally, the resultant solution was freeze-

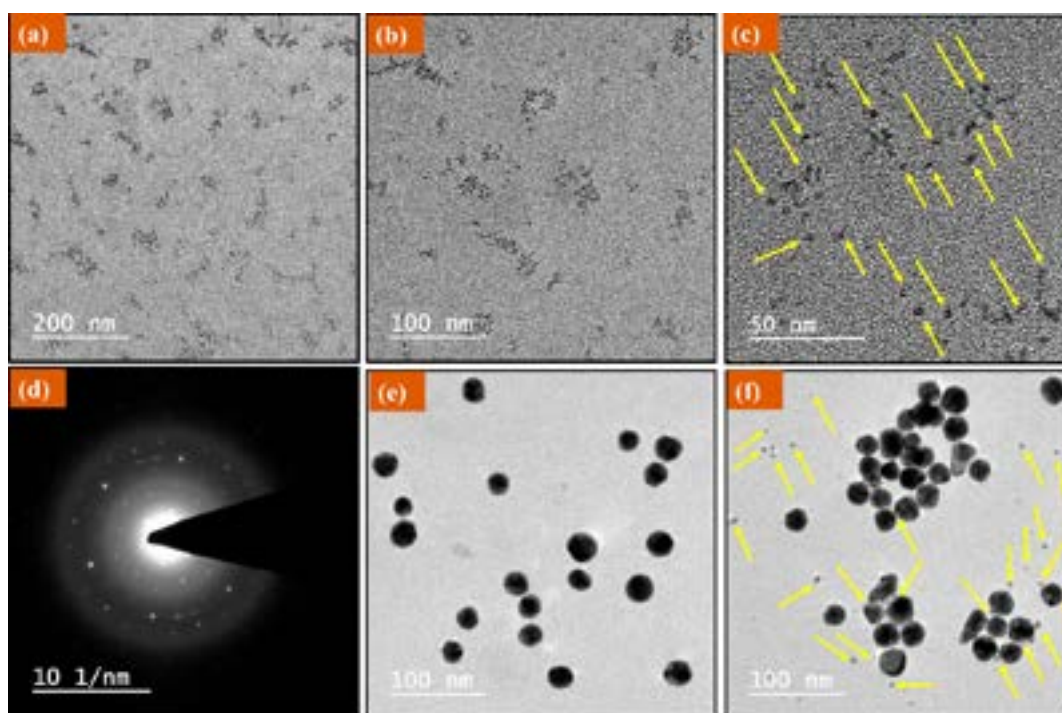


Figure 2. (a–c) TEM images of synthesized amine-N-GQDs at different scales; (d) SAED pattern of amine-N-GQDs; (e) TEM image of AuNPs; (f) TEM image of the amine-N-GQDs@AuNPs composite.

dried for 48 h to obtain the semisolid yellow amine-N-GQDs, which was further dispersed in deionized water to obtain the amine-N-GQDs stock solution and stored at 4 °C until further use. [Scheme S1](#) illustrates the amine-N-GQDs synthesis process using the bottom-up hydrothermal method. A similar procedure was carried out for the synthesis of GQDs without adding the DETA solution.

2.2. Preparation of Anti-NSE/Amine-N-GQDs Conjugate. For this, the procedure has been adapted from Kumar et al.³⁵ First, monoclonal neuron-specific enolase antibodies (anti-NSE) were activated utilizing the standard EDC-NHS coupling chemistry. For this, 150 μ L of anti-NSE (50 μ g mL⁻¹), 75 μ L of 0.2 M EDC and 0.05 M NHS were mixed and incubated at room temperature for 30 min, where NHS activated the –COOH groups present on the Fc region of the anti-NSE antibody and EDC acted as the coupling agent. The activated antibody solution was added to the diluted amine-N-GQDs (100 μ g mL⁻¹) solution (1:1 v/v) and allowed to incubate at room temperature for an additional 2 h duration. The anti-NSE/amine-N-GQDs conjugate was obtained through the amide bond formation between the –COOH groups of anti-NSE and –NH₂ groups of amine-N-GQDs, and further characterized by UV–vis, zeta potential, and FTIR studies (details in [Supporting Information, Figure S2a–c](#)). The calculated adhesion efficiency was found to be 88.13% indicating the high ability of amine-N-GQDs for the development of efficient fluorescent biosensor (details in [Supporting Information, Figure S2d](#)).

2.3. Procedure and Mechanism of Fluorescent Biosensor for NSE Detection. The mechanism of anti-NSE/amine-N-GQDs@AuNPs based fluorescent biosensor has been schematically illustrated in [Figure 1](#). The anti-NSE/amine-N-GQDs conjugate emits strong blue fluorescence under the exposure of 360 nm (“ON” state), which is quenched by the ultrahigh quenching efficiency of AuNPs (acceptor). In AuNPs, there are free conduction band electrons that provide dipole vectors on the surface of AuNPs, thereby accepting the donor energy.^{4,36} Also, the larger surface area of AuNPs provides efficient energy transfer by using the concept of multiple-donor–single-acceptor configuration. Additionally, AuNPs do not possess definite dipole moment; therefore, energy transfer to the AuNPs can occur from the donor in any orientation. Moreover, AuNPs’ broad absorption cross-sections, particularly close to their Plasmon resonance, enrich their performance as energy acceptors.^{4,36,37}

An optimized amount of anti-NSE/amine-N-GQDs conjugate was mixed with AuNPs (disclosure subject to acquired patent clauses, Indian patent, Application No. 202011010110) and PL emission spectra were recorded at room temperature to observe the quenching effect (“OFF” state). Further, 50 μ L of each antigen concentration was added to anti-NSE/amine-N-GQDs@AuNPs solution. The resultant solution was diluted to 1 mL with phosphate buffer saline (PBS) solution (pH 7.4) and incubated for the optimized duration of 16 min. Subsequently, PL emission spectra were measured to observe the fluorescence intensity recovery with increasing NSE antigen concentration. Upon the addition of NSE antigen, the distance between anti-NSE/amine-N-GQDs conjugate and AuNPs increases because NSE antigen binds explicitly with the anti-NSE antibody due to specific antigen–antibody interactions forming a NSE/anti-NSE/amine-N-GQDs@AuNPs immunocomplex. The formed complex obstructs the energy transfer process because the antigen–antibody interactions are stronger than the adsorption between anti-NSE/amine-N-GQDs conjugate and AuNPs, resulting in the restoration of fluorescence with the addition of increasing NSE antigen concentration (“ON” state).

3. RESULTS AND DISCUSSION

3.1. Morphological and Structural Characterizations.

The obtained amine-N-GQDs have been characterized for the morphological, structural, and size distribution analysis utilizing the TEM ([Figure 2a–c](#)) and XRD analysis ([Figure S1](#)). The corresponding TEM images at different scales denote that the obtained amine-N-GQDs are nonaggregated and uniformly distributed QDs with an average size of \sim 3 nm. The selected area electron diffraction (SAED) pattern ([Figure 2d](#)) shows the characteristic diffraction pattern with bright points suggesting the excellent crystallinity of synthesized amine-N-GQDs.³⁸ Similarly, the XRD pattern of amine-N-GQDs ([Figure S1](#)) exhibited a broad peak around 25.2°, which is consistent with 002 planes of graphene. The TEM image ([Figure 2e](#)) indicates that the AuNPs are also well distributed and round-shaped nanoparticles with an average size of \sim 20

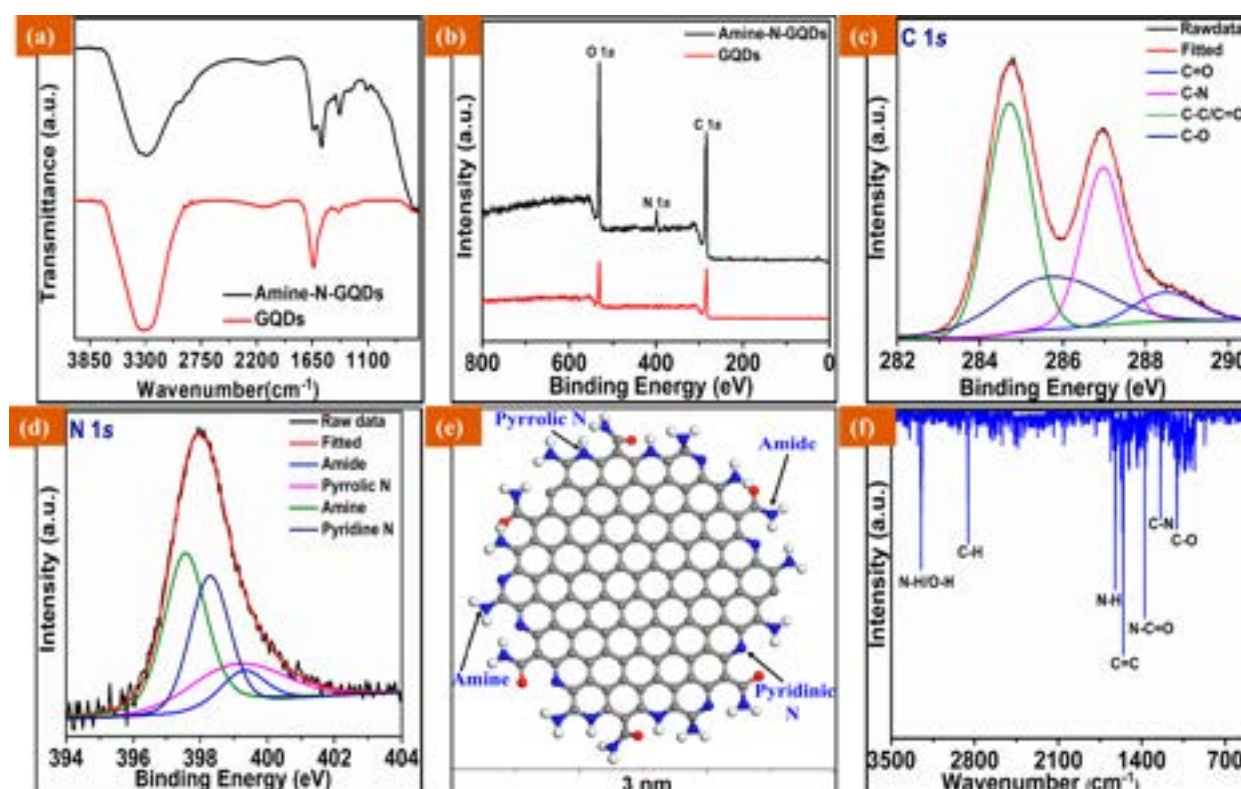


Figure 3. (a) FTIR spectra of synthesized GQDs (red line) and amine-N-GQDs (black line); (b) full scan XPS spectra of synthesized GQDs and amine-N-GQDs; (c) deconvoluted C 1s spectra of amine-N-GQDs; (d) deconvoluted N 1s spectra of amine-N-GQDs; (e) theoretically optimized structure and (f) theoretically calculated FTIR spectrum of amine-N-GQDs.

nm. Figure 2f shows the TEM image of the amine-N-GQDs@AuNPs composite. Smaller sized amine-N-GQDs were found to surround the larger AuNPs forming a satellite structure. Further, the cytotoxicity studies of amine-N-GQDs were carried out using the MTT assay on both normal lung (L-132) and cancer (A549) cell lines (details in [Supporting Information, Figure S3](#)).

3.1.1. Fourier Transform Infrared (FTIR) and X-ray Photoelectron Spectroscopy (XPS). FTIR was performed to determine the presence of different functional groups on bare GQDs and amine-N-GQDs (Figure 3a). In both spectra, the bands obtained around 1115 cm⁻¹ and 1556 cm⁻¹ are assigned to C–O stretching and aromatic C=C ring stretching vibrations, respectively.^{39,40} Similarly, bands obtained between 2800 and 3000 cm⁻¹ are attributed to C–H stretching vibrations for both spectra. In the case of GQDs, stretching vibrations related to only O–H groups (3000–3400 cm⁻¹) were obtained, whereas in amine-N-GQDs, N–H amine/amide stretching vibrations along with O–H vibrations were obtained.⁴⁰ In amine-N-GQDs spectra, additional peaks were acquired around 1250 and 1380 cm⁻¹ due to C–N in-plane and N–C=O stretching, respectively.³⁹ In the case of bare GQDs, the obtained shoulder peak around 1740 cm⁻¹ and intense peak around 1650 cm⁻¹ indicate the presence of carboxylic groups. However, in amine-N-GQDs, the dissipation of these peaks can be attributed to the combined effect of N–H bending vibrations and amide-carbonyl (–NH–C=O) vibrations due to the formation of amide bonds through the interaction of –COOH group of GQDs as Lewis base.⁴⁰ The presence of additional amine and amide functionalities in amine-N-GQDs FTIR spectra verified its successful *in situ* amine functionalization.

Further, XPS measurements were performed to investigate the surface chemistry of GQDs and amine-N-GQDs. Figure 3b shows the full scan XPS spectra of GQDs and amine-N-GQDs. It can be observed that only carbon C 1s (~284 eV) and oxygen O 1s (~532 eV) peaks are present in GQDs, whereas nitrogen N 1s peaks (~400 eV) along with carbon and oxygen peaks are present in amine-N-GQDs. Further, for the detailed analysis, the C 1s high-resolution XPS spectra (Figure 3c) were deconvoluted into four main peaks, present at the binding energy of 284.71, 285.70, 286.96, and 288.49 eV, which can be attributed to sp² (C–C/C=C) domains of graphitic structures, C–O, C–N, and C=O functional groups, respectively.^{39–41} It can be assumed that the N-doping of GQDs through the interaction with DETA molecules results in the appearance of C–N bonds by converting carbonyl (C=O) and epoxy (C–O) groups into amine/amide functionalities. Similarly, in the deconvoluted N 1s spectra (Figure 3d), four main peaks present at the binding energy of 399.4, 399.1, 398.3, and 397.5 eV can be assigned to amide-carbonyl (–NH–C=O), pyrrolic (C2–N–H), pyridinic (C–N–C), and amine (–NH₂) functional groups, respectively.^{28,39,40,42} Besides, quantitative XPS results show the presence of 59.54% carbon and 18.65% nitrogen, signifying that the prepared amine-N-GQDs are carbon-rich and sufficiently nitrogen-doped.

3.2. Molecular Simulations. For amine-N-GQDs structure optimization and in-depth analysis of FTIR and XPS spectra, to explore the presence of possible nitrogen doping (N-doping) and amine functionalization sites, molecular simulations were performed using Material Studio software of Dassault Systems (previously Accelrys Inc.).⁴³ The geometrical structure of amine-N-GQDs crystals was optimized using the BFGS algorithm after aptly selecting convergence

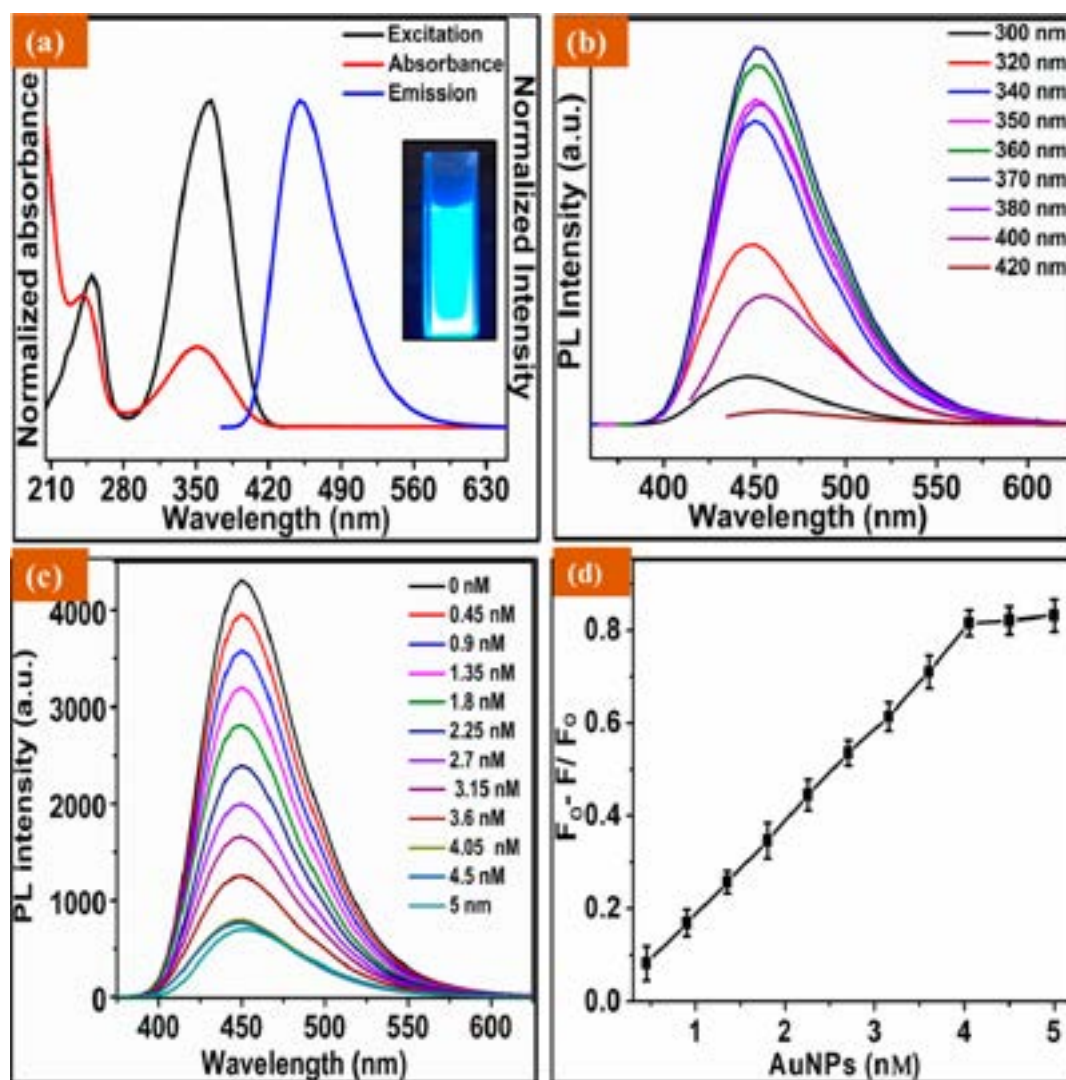


Figure 4. (a) Excitation (black line), emission (blue line), and absorbance (red line) spectra of amine-N-GQDs (inset: intense and bright blue colored fluorescence of amine-N-GQDs under the irradiation of 365 nm UV light); (b) PL spectra of amine-N-GQDs at different excitation wavelengths; (c) fluorescence spectra of anti-NSE/amine-N-GQDs nanoprobe with increasing quencher (AuNPs) concentration (0–5 nM from top to bottom); (d) quenching efficiency (QE) induced by different concentration of AuNPs.

tolerance parameters (maximum force, 0.05 eV/Å; energy, 2.0×10^{-5} eV/atom; maximum stress, 0.1 GPa; maximum displacement, 0.002 Å; maximum iterations, 100). The successfully optimized and relaxed atomic structure of amine-N-GQDs (Figure 3e) was compared with experimentally characterized structures for the validation of size, N-doping sites, and surface functionalization. It can be observed from Figure 3e that the size of the computationally optimized structure (~3 nm) is in good accordance with the TEM results of as-synthesized amine-N-GQDs. Also, the various N-doping sites (pyrrolic (C2–N–H), pyridinic (C–N–C) N), amine, and amide functionalities observed from the theoretical structure are in decent agreement with XPS results.

Next, the FTIR spectrum of the theoretically optimized amine-N-GQDs structure (Figure 3f) was computationally calculated using vibrational analysis tools in Material Studio software. The peaks obtained at 2854 and 3252 cm^{-1} correspond to the stretching vibration of C–H and N–H amine/amide bonds, respectively. The appearance of a characteristic peak at 1621 cm^{-1} can be attributed to the bending vibration of N–H, and –NH–C=O. The additional

peaks observed at 1554, 1372, 1242, and 1102 cm^{-1} can be ascribed to stretching vibrations of C=C present in GQDs framework, N–C=O, C–N in-plane stretching, and C–O, respectively. Interestingly, all the peaks observed in theoretically calculated FTIR spectrum for their respective bonds existing in the optimized structure are in good agreement with experimental FTIR results. From both experimental and theoretical results, it can be stated that DETA treatment during the hydrothermal synthesis results in the substitutional N-doping at the edge sites of GQDs. Moreover, the presence of amine and amide functionalities verified the successful surface functionalization.

3.3. Optical Characterizations. The absorption spectra of amine-N-GQDs (Figure 4a) exhibit an absorbance band around 240 nm, which might be ascribed to π – π^* transition of C=C aromatic sp^2 atoms and the construction of multiple polyaromatic chromophores.⁴¹ It has been reported that in the case of bare GQDs, the absorption peak obtained between 320 and 350 nm is generally assigned to n – π^* transitions of C=O bonds, which disappears immediately after the reduction.²⁸ To verify this, we also performed the reduction of amine-N-GQDs

with NaBH₄ and further measured the absorbance and PL spectra. However, no significant change was observed in both spectra after the reduction reaction (Figure S4), signifying that the band present around 350 nm is not only because of n- π^* transitions of C=O but also related to the C-N/C=N transitions due to N-doping of GQDs.²⁸ The absolute QY of synthesized amine-N-GQDs was obtained as high as 76.83% compared to pristine GQDs (14.57%), which is favorable for working as the energy donor. The high QY can be assigned to the combined effect of N-doping and amine functionalization of GQDs. N-doping introduces additional surface energy state and more active sites, which promotes radiative recombination resulting in improved fluorescence.²⁷ Furthermore, the surface functionalization converts the -COOH and epoxy groups of GQDs to -CNHR and -CONHR. These groups result in suppression of nonradiative electron-hole recombination and thereby enrich intrinsic state emission.¹⁹ The PL spectra of amine-N-GQDs exhibited a broad emission band centered around 450 nm at the excitation wavelengths of 360 nm (Figure 4a). The picture in the inset of Figure 4a revealed the intense and bright blue colored fluorescence of amine-N-GQDs aqueous solution under the exposure of 365 nm UV light. Further, the results of the photoluminescence (PL) spectra of amine-N-GQDs (Figure 4b) under different excitation wavelengths (300–420 nm) demonstrated that the emission spectra are nearly excitation independent. The PL intensity was found to increase in the range of 300 to 370 nm and then gradually decreases.

3.4. Energy Transfer between Anti-NSE/Amine-N-GQDs and AuNPs. The selection of appropriate donor-acceptor pair has been found to be very important for highly efficient energy transfer. Moreover, it has been reported that there should be a substantial spectral overlap between the absorption spectrum of the acceptor and the emission spectrum of the donor.^{44,45} Figure S5 indicated that the absorption spectra of AuNPs significantly overlap with the emission spectra of anti-NSE/amine-N-GQDs, ensuring that highly efficient energy transfer occurs between the selected donor-acceptor pair. Next, the anti-NSE/amine-N-GQDs conjugate was incubated with a series of AuNPs concentration (0–5 nM). Then the PL spectra of anti-NSE/amine-N-GQDs@AuNPs nanocomplex were recorded for this series of quencher concentrations. It has been observed that the PL intensity of anti-NSE/amine-N-GQDs conjugate gradually decreases as AuNPs concentration increases without any shift in peak position (Figure 4c). This quenching has been induced by the dipole-surface interactions between anti-NSE/amine-N-GQDs conjugate and AuNPs, which brings them in close proximity to transfer the excited state energy to AuNPs.¹⁷ This self-assembled anti-NSE/amine-N-GQDs@AuNPs nanocomplex acts as a fluorescent nanoprobe for the target biomarker detection. The quenching efficiency (QE) has been calculated using eq 1:

$$QE = F_0 - F/F_0 \quad (1)$$

where F_0 is the PL intensity of anti-NSE/amine-N-GQDs conjugate solution incubated with only PBS (no quencher), and F is the PL intensity of anti-NSE/amine-N-GQDs conjugate in the presence of quencher. The maximum quenching efficiency (Figure 4d) was calculated to be 81.5% with 4.05 nM AuNPs concentration. After that, the PL intensity was found almost unchanged, signifying the completion of the quenching between anti-NSE/amine-N-

GQDs and AuNPs. Thus, 4.05 nM was selected as the optimal concentration and used for further experiments. Further, to analyze the quenching mechanism, the Stern-Volmer plot, that is, the relative change in fluorescence intensity (F_0/F) as a function of quencher concentration [AuNPs] has been studied (Figure S6). This plot has been found to be nonlinear with upward curvature signifying that both static and dynamic quenching processes are involved in the sensing system. Next, time-resolved PL spectroscopy was performed to investigate the dynamics of energy transfer for the selected donor-acceptor pair (Figure S7). It was observed that the fluorescence lifetime of anti-NSE/amine-N-GQDs conjugate decreases significantly after the addition of AuNPs, specifying the energy transfer process from the biofunctionalized conjugate to AuNPs.^{17,46} The energy transfer efficiency between the selected pair was calculated using eq 2:

$$\phi_E = 1 - \frac{\tau_{DA}}{\tau_D} \quad (2)$$

where τ_D is the decay lifetime of anti-NSE/amine-N-GQDs conjugate without acceptor (AuNPs), and τ_{DA} is the lifetime of anti-NSE/amine-N-GQDs conjugate with energy acceptor. The energy transfer efficiency between the selected pair was obtained to be 42.9%. This nonradiative energy transfer between donor-acceptor pair can be modeled as dipole to surface energy transfer and has been explained by following the NSET mechanism as described previously.^{17,18} The critical distance R_0 , where energy transfer efficiency is 50%, was calculated using the Persson-Lang model (eq 3):

$$R_0 = \left[\frac{0.225c^3\Phi_D}{\omega_D^2\omega_Fk_f} \right]^{1/4} \quad (3)$$

where Φ_D is the donor quantum yield (0.76) without acceptor, c is the speed of light, ω_D is the donor angular frequency ($4.2 \times 10^{15} \text{ s}^{-1}$), and k_f ($1.2 \times 10^{10} \text{ cm}^{-1}$) and ω_F ($8.4 \times 10^{15} \text{ s}^{-1}$) are the Fermi vector and angular frequency of bulk gold, respectively. The critical distance R_0 for the selected pair was obtained to be 7.1 nm. Subsequently, the distance between the chosen donor-acceptor pair (r) was calculated using eq 4:

$$r = R_0 \left[\frac{\tau_{DA}}{\tau_D - \tau_{DA}} \right]^{1/4} \quad (4)$$

where τ_D is the decay lifetime of anti-NSE/amine-N-GQDs conjugate without acceptor (AuNPs), and τ_{DA} is the lifetime of anti-NSE/amine-N-GQDs conjugate with the acceptor. The distance (r) was obtained to be 8.8 nm. The calculated distance was obtained well within the limit of forming NSET pair for energy transfer.^{17,47}

3.5. Detection of NSE Biomarker. First, to realize the NSE biomarker detection, the effect of pH on the PL intensity of anti-NSE/amine-N-GQDs conjugate has been investigated (details in Supporting Information, Figure S8). Then different concentrations of the NSE antigen (0.1 pg mL^{-1} to 1000 ng mL^{-1}) were prepared by diluting the obtained stock solution. After that, the anti-NSE/amine-N-GQDs@AuNPs nanocomplex solution was optimized for the minimum response time required to recover the quenched fluorescence intensity. Fifty microliters of NSE antigen (1 ng mL^{-1}) was added into the anti-NSE/amine-N-GQDs@AuNPs nanocomplex solution. After the NSE antigen was added, the nanocomplex solution was allowed to incubate for the different time duration (2 to 32

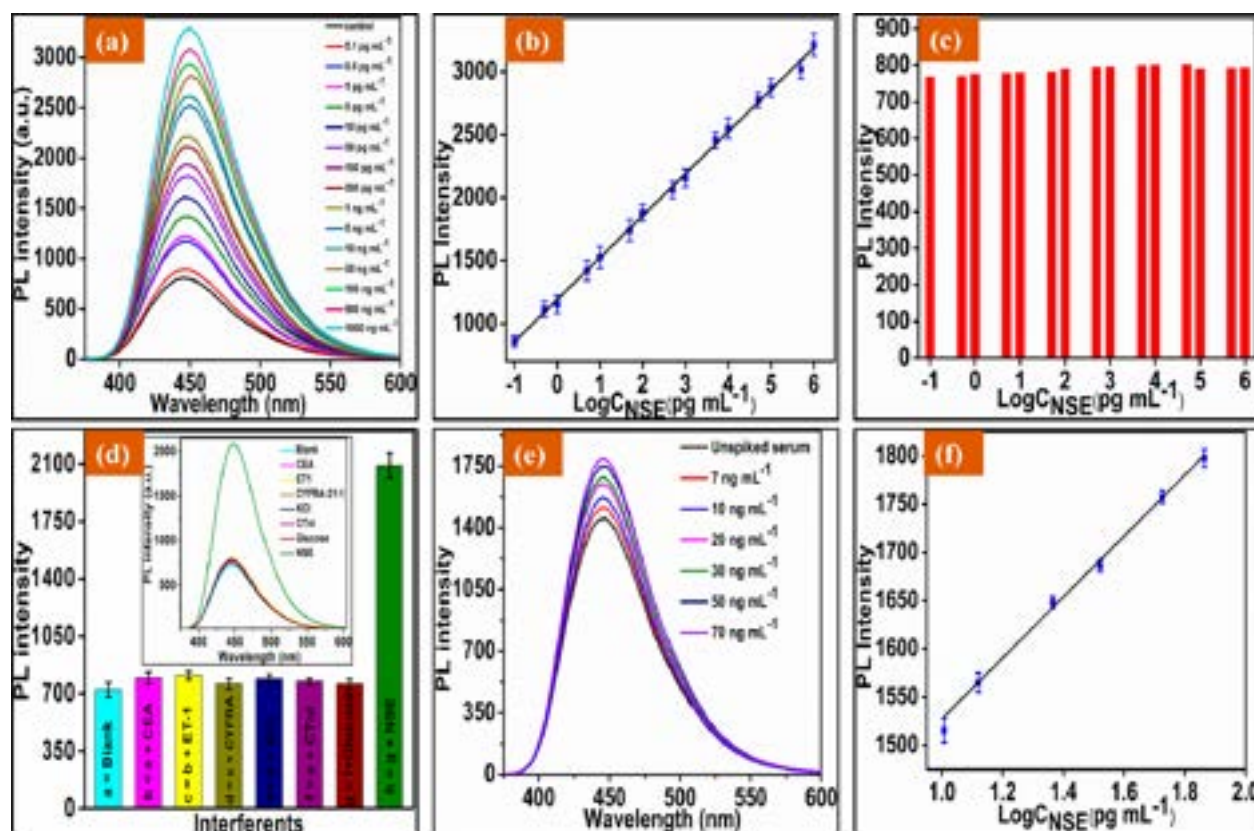


Figure 5. (a) Fluorescence response studies of anti-NSE/amine-N-GQDs@AuNPs nanoprobe as a function of NSE antigen concentration (0.1 pg mL^{-1} to 1000 ng mL^{-1} from bottom to top); (b) calibration curve indicating the linear relationship between log concentration of NSE and PL intensity of the nanoprobe; (c) control experiment of amine-N-GQDs@AuNPs as a function of log concentration of NSE antigen and PL intensity; (d) selectivity studies of anti-NSE/amine-N-GQDs@AuNPs nanoprobe with different interferents (inset shows their corresponding PL spectra); (e) PL curves indicating the fluorescence response of anti-NSE/amine-N-GQDs@AuNPs nanoprobe toward spiked serum samples ($7, 10, 20, 30, 50$, and 70 ng mL^{-1}); (f) calibration curve for the spiked serum samples indicating the linear relationship between log concentration of NSE and PL intensity of the nanoprobe.

min) to have efficient immunoreaction and obstruction in the energy transfer process to recover the fluorescence. Figure S9 indicates that the PL intensity recovered gradually, reaching the highest value at 16 min, after which no significant increase was obtained in the PL intensity. Therefore, the optimum response time has been selected to be 16 min for the NSE detection, during which the immunoreaction attains the steady-state condition. Figure 5a shows the PL response of the anti-NSE/amine-N-GQDs@AuNPs nanocomplex for the different NSE antigen concentrations (0.1 pg mL^{-1} to 1000 ng mL^{-1}). Fluorescence intensity of anti-NSE/amine-N-GQDs conjugate was found to recover linearly with increasing NSE antigen concentration (Figure 5b) and can be described by the eq 5:

$$I = 333.20 \log_{10} \text{NSE (pg mL}^{-1}) + 1190.84$$

Regression coefficient $R^2 = 0.998$ (5)

The PL intensity recovery can be attributed to the formation of immunocomplex arising due to the specific interaction of NSE antigen with anti-NSE antibody, which increases the distance between anti-NSE/amine-N-GQDs donor and AuNPs quencher resulting in the obstruction of the energy transfer process and hence gradual recovery of fluorescence.^{48,49} Further, the limit of detection (LOD) was found to be 0.09 pg mL^{-1} calculated using the eq 6:

$$\text{LOD} = \frac{3\sigma}{S} \quad (6)$$

where σ is the standard deviation, and S is the sensitivity of the fluorescent biosensor calculated using the slope of the calibration curve.

3.6. Control Experiment, Selectivity, and Reproducibility Studies. A control experiment was conducted to investigate the PL response of amine-N-GQDs@AuNPs nanocomplex as a function of NSE antigen (0.1 pg mL^{-1} to 1000 ng mL^{-1}). No significant recovery in the fluorescence of amine-N-GQDs was obtained with increasing NSE antigen concentration (Figure 5c), signifying that the NSE antigen does not interact with the amine-N-GQDs@AuNPs to form the antigen–antibody immunocomplex. Therefore, there will be no obstruction in the energy transfer process to recover the fluorescence. Next, the selectivity study of the fluorescent biosensor (Figure 5d) was performed by incubating the amine-N-GQDs@AuNPs nanocomplex with different interfering substances such as carcinoembryonic antigen (CEA), endo-thelin-1 (ET-1), cardiac troponin-I (cTnI), potassium chloride (KCl), cytokeratin-19 fragment (CYFRA-21-1), and glucose known to be present in serum samples. The nanocomplex was incubated with $50 \mu\text{L}$ of each interferant one by one in the same solution, and their corresponding PL spectra were measured. A negligible change in the magnitude of fluorescence intensity was observed in the presence of these

Table 1. Characteristics of Different Biosensing Platforms and Detection Techniques Used for NSE Detection

sr. no.	biosensing platform used	detection technique	detection range (ng mL ⁻¹)	LOD	time (min)	ref
1.	anti-NSE/ZnCdHgSe QDs/PDPIT/ITO	Photoelectrochemical	0.001–100	0.2 pg mL ⁻¹	30	50
2.	anti-NSE/Cs nanoAu/APTES/PBSiO ₂ /GCE	Amperometric	0.25–75.0	0.08 ng mL ⁻¹	35	51
3.	AP-anti-IgG/AuNPs/anti-NSE/NSESNTs/GCE	Electrochemical	0.10–2000	0.03 ng mL ⁻¹	60	52
4.	anti-NSE/Au–Gra/NiHCFNPs/AuNCs/GCE	Electrochemical	0.001–100	0.3 pg mL ⁻¹	30	53
5.	PPD-GR/AuNPs/anti-NSE/SPE	Electrochemical	1–1000	0.3 ng mL ⁻¹	60	3
6.	Anti-NSE/NSE/anti-NSE-biotin/streptavidin/FITC/QDs	Fluorescence	3–100	1.0 ng mL ⁻¹		54
7.	CaCO ₃ /AuNCs hybrid	Fluorescence Electrochemical	0.005–1 0.0005–2	2.0 pg mL ⁻¹ 0.1 pg mL ⁻¹	30	55
8.	FITC-anti-NSE/ALP-NSE/anti-FITC-MB	Chemiluminescence	0–300	0.2 ng mL ⁻¹		56
9.	anti-NSE/DA/TiO ₂ /FTO	Photoelectrochemical	0.1–1000	0.05 ng mL ⁻¹	30	57
10.	NH ₂ -G/Thi/AuNPs POCT	Wireless POCT	1–500	10 pg mL ⁻¹	18	58
11.	anti-NSE/amine-N-GQDs @AuNPs	NSET	0.0001–1000	0.09 pg mL ⁻¹	16	This work

interferants compared to the blank (amine-N-GQDs@AuNPs). The variation (recovery) in the fluorescence intensity was found to be less than 5%. However, upon the addition of target NSE, antigen fluorescence intensity recovered significantly, validating the good selectivity of fabricated biosensor toward NSE detection. Also, the selectivity coefficient (SC) for each interferant was found to be ~ 1 , calculated using eq 7:

$$SC = \frac{I_{C+I}}{I_C} \quad (7)$$

where I_{C+I} is the magnitude of PL intensity in the presence of the interferant, while I_C is the magnitude of PL intensity in the absence of the interferant. The reproducibility of the fluorescent biosensor was investigated by measuring the fluorescence recovery of six different nanoprobe (anti-NSE/amine-N-GQDs@AuNPs) fabricated under similar conditions and incubated with same NSE antigen concentration (1 ng mL⁻¹). Similar results with a calculated relative standard deviation (% RSD) of 1.85 from all of the nanoprobe signifies the high reproducibility of the fabricated biosensor (Figure S10).

3.7. Real Sample Analysis. In this context, first, the blood was collected in a sterilized tube from a healthy person after taking his written consent and approval from the institutional Ethical and Biosafety committee (BT/IHEC-IITR/2019/7525) and further centrifuged at 4000 rpm to obtain the clear serum. After that, to quantify the feasibility of the fluorescent biosensor in real samples, serum of a healthy human was spiked with six different NSE antigen concentrations (7, 10, 20, 30, 50, and 70 ng mL⁻¹), and the response was measured using PL (Figure 5e). Similar to the previous experiment, the nanocomplex solution (anti-NSE/amine-N-GQDs@AuNPs) was incubated for the optimized incubation time of 16 min after addition of NSE spiked serum samples to have efficient immunoreaction. A similar kind of trend, indicating increase (recovery) in the fluorescence intensity with increasing NSE concentration, has been obtained for the spiked serum samples. The calibration curve (Figure 5f) shows a linear relationship between PL intensity and six NSE antigen spiked serum samples and fit according to eq 8:

$$I = 315.83 \log_{10} \text{NSE (pg mL}^{-1}\text{)} + 1211.79$$

$$\text{Regression coefficient } R^2 = 0.992 \quad (8)$$

The % recovery of NSE in the serum samples has been calculated utilizing eq 9 and has been indicated in Table S1:

$$\% \text{ recovery} = \frac{y_1 - y_0}{y_s} \times 100 \quad (9)$$

where y_0 and y_1 are the obtained concentrations of the NSE in unspiked and spiked samples from the calibration plot of standard samples, and y_s is the actual concentration of spiked NSE. The fluorescent biosensor revealed an average recovery of 94.69% for NSE antigen in spiked serum samples, signifying the high efficiency of the fluorescent biosensor for NSE detection in real samples. Finally, comparison of the proposed fluorescent biosensor with the previously reported biosensors for NSE detection has been shown in Table 1.

4. CONCLUSIONS

We have demonstrated the fabrication and application of fluorescent biosensor for the quantitative and ultrasensitive NSE detection utilizing biofunctionalized graphene quantum dots as an energy donor and AuNPs as the acceptor. The bottom-up hydrothermal method provided uniform and small-sized (~ 3 nm) amine-N-GQDs with excellent optical properties, namely high absolute QY $\approx 76.83\%$, excitation independent, blue colored, strong and stable fluorescence, longer fluorescence decay lifetime (13.1 ns). The structure of synthesized amine-N-GQDs has been successfully estimated through the molecular simulation studies. Both theoretical and experimental characterization tools verified the successful N-doping and amine functionalization. The MTT assay results provided the high cell viability (81.5% for A549 and 84.5% for L-132) even at higher concentration (1000 $\mu\text{g mL}^{-1}$). Efficient quenching efficiency of 81.5% and energy transfer efficiency of 42.9% have been obtained with the selected donor–acceptor pair. The developed NSE/anti-NSE/amine-N-GQDs@AuNPs fluorescent turn-on biosensor was successfully utilized for NSE biomarker detection with remarkable biosensing parameters including fast response time (16 min), wider linear detection range (0.1 pg mL⁻¹ to 1000 ng mL⁻¹), excellent selectivity, and remarkable low detection limit (0.09 pg mL⁻¹). The

fluorescent biosensor also exhibited excellent performance in real samples, with an average recovery of 94.69%. This amine-N-GQDs based fluorescent biosensor development opens a new window for the widespread utilization of evolving zero-dimensional fluorescent materials in various biomedical applications including biosensing, bioimaging, gene delivery, drug delivery, and 3D printed implantable biochip.

■ ASSOCIATED CONTENT

Supporting Information

The Supporting Information is available free of charge at <https://pubs.acs.org/doi/10.1021/acsabm.0c00427>.

Chemicals and reagents, instrumentation, synthesis of gold nanoparticles (AuNPs), characterizations of bio-functionalized conjugate, calculation of adhesion efficiency, cytotoxicity studies, PL emission and UV–vis spectra of amine-N-GQDs before and after reduction, overlap between absorption and emission spectra, Stern–Volmer plot, time resolved PL spectroscopy studies, pH study, response time and reproducibility study graphs, estimation of NSE in spiked serum samples (PDF)

■ AUTHOR INFORMATION

Corresponding Author

Gopinath Packirisamy – Department of Biotechnology and Centre for Nanotechnology, Indian Institute of Technology Roorkee, Roorkee, Uttarakhand 247667, India; orcid.org/0000-0003-1379-1203; Phone: +91-1332-285650; Email: gopi@bt.iitr.ac.in, genegopi@gmail.com; Fax: +91-1332-273560

Authors

Ashish Kalkal – Department of Biotechnology, Indian Institute of Technology Roorkee, Roorkee, Uttarakhand 247667, India; orcid.org/0000-0002-4342-1193

Rangadhar Pradhan – Centre for Nanotechnology, Indian Institute of Technology Roorkee, Roorkee, Uttarakhand 247667, India; orcid.org/0000-0002-9283-4955

Sachin Kadian – Department of Polymer and Process Engineering, Indian Institute of Technology Roorkee, Roorkee, Uttarakhand 247667, India; orcid.org/0000-0002-2804-1109

Gaurav Manik – Department of Polymer and Process Engineering, Indian Institute of Technology Roorkee, Roorkee, Uttarakhand 247667, India; orcid.org/0000-0003-2501-1737

Complete contact information is available at: <https://pubs.acs.org/doi/10.1021/acsabm.0c00427>

Author Contributions

[†]These authors contributed equally to work.

Notes

The authors declare no competing financial interest.

■ ACKNOWLEDGMENTS

This work was supported by the Department of Biotechnology (No. BT/PR25095/NER/95/1011/2017), Government of India. AK and SK are grateful to the MHRD, Government of India, for the fellowship. The authors would like to thank Prof. Rishi Pal Chauhan, Head, Department of Physics, National Institute of Technology Kurukshetra, for permitting

to use Material Studio software. The authors are thankful to the Department of Biotechnology, Centre of Nanotechnology, IIT Roorkee, India, for providing the required infrastructure to perform the research work and Institute Instrumentation center for providing various characterization facilities.

■ REFERENCES

- (1) Stovold, R.; Blackhall, F.; Meredith, S.; Hou, J.; Dive, C.; White, A. Biomarkers for small cell lung cancer: Neuroendocrine, epithelial and circulating tumour cells. *Lung Cancer* **2012**, *76* (3), 263–268.
- (2) Arya, S. K.; Bhansali, S. Lung Cancer and Its Early Detection Using Biomarker-Based Biosensors. *Chem. Rev.* **2011**, *111* (11), 6783–6809.
- (3) Amani, J.; Maleki, M.; Khoshroo, A.; Sobhani-Nasab, A.; Rahimi-Nasrabadi, M. An electrochemical immunosensor based on poly p-phenylenediamine and graphene nanocomposite for detection of neuron-specific enolase via electrochemically amplified detection. *Anal. Biochem.* **2018**, *548*, 53–59.
- (4) Shi, J.; Tian, F.; Lyu, J.; Yang, M. Nanoparticle based fluorescence resonance energy transfer (FRET) for biosensing applications. *J. Mater. Chem. B* **2015**, *3* (35), 6989–7005.
- (5) Youssef, S.; Zhang, S.; Ai, H.-w. A Genetically Encoded, Ratiometric Fluorescent Biosensor for Hydrogen Sulfide. *ACS Sensors* **2019**, *4* (6), 1626–1632.
- (6) Lau, D.; Walsh, J. C.; Peng, W.; Shah, V. B.; Turville, S.; Jacques, D. A.; Böcking, T. Fluorescence Biosensor for Real-Time Interaction Dynamics of Host Proteins with HIV-1 Capsid Tubes. *ACS Appl. Mater. Interfaces* **2019**, *11* (38), 34586–34594.
- (7) Della Ventura, B.; Gelzo, M.; Battista, E.; Alabastri, A.; Schirato, A.; Castaldo, G.; Corso, G.; Gentile, F.; Velotta, R. Biosensor for Point-of-Care Analysis of Immunoglobulins in Urine by Metal Enhanced Fluorescence from Gold Nanoparticles. *ACS Appl. Mater. Interfaces* **2019**, *11* (4), 3753–3762.
- (8) Fu, Y.; Chen, T.; Wang, G.; Gu, T.; Xie, C.; Huang, J.; Li, X.; Best, S.; Han, G. Production of a fluorescence resonance energy transfer (FRET) biosensor membrane for microRNA detection. *J. Mater. Chem. B* **2017**, *5* (34), 7133–7139.
- (9) Wang, G.; He, P.; Xu, A.; Guo, Q.; Li, J.; Wang, Z.; Liu, Z.; Chen, D.; Yang, S.; Ding, G. Promising Fast Energy Transfer System Between Graphene Quantum Dots and the Application in Fluorescent Bioimaging. *Langmuir* **2019**, *35* (3), 760–766.
- (10) Das, P.; Sedighi, A.; Krull, U. J. Cancer biomarker determination by resonance energy transfer using functional fluorescent nanoprobe. *Anal. Chim. Acta* **2018**, *1041*, 1–24.
- (11) Ma, F.; Li, C.-c.; Zhang, C.-y. Development of quantum dot-based biosensors: principles and applications. *J. Mater. Chem. B* **2018**, *6* (39), 6173–6190.
- (12) Wolfbeis, O. S. Materials for fluorescence-based optical chemical sensors. *J. Mater. Chem.* **2005**, *15* (27–28), 2657–2669.
- (13) Yang, S.; Sun, J.; Li, X.; Zhou, W.; Wang, Z.; He, P.; Ding, G.; Xie, X.; Kang, Z.; Jiang, M. Large-scale fabrication of heavy doped carbon quantum dots with tunable-photoluminescence and sensitive fluorescence detection. *J. Mater. Chem. A* **2014**, *2* (23), 8660–8667.
- (14) Biju, V.; Itoh, T.; Ishikawa, M. Delivering quantum dots to cells: bioconjugated quantum dots for targeted and nonspecific extracellular and intracellular imaging. *Chem. Soc. Rev.* **2010**, *39* (8), 3031–3056.
- (15) Sun, J.; Yang, S.; Wang, Z.; Shen, H.; Xu, T.; Sun, L.; Li, H.; Chen, W.; Jiang, X.; Ding, G.; Kang, Z.; Xie, X.; Jiang, M. Ultra-High Quantum Yield of Graphene Quantum Dots: Aromatic-Nitrogen Doping and Photoluminescence Mechanism. *Particle & Particle Systems Characterization* **2015**, *32* (4), 434–440.
- (16) Yang, S.; Sun, J.; He, P.; Deng, X.; Wang, Z.; Hu, C.; Ding, G.; Xie, X. Selenium Doped Graphene Quantum Dots as an Ultrasensitive Redox Fluorescent Switch. *Chem. Mater.* **2015**, *27* (6), 2004–2011.
- (17) Chen, C.; Midelet, C.; Bhuckory, S.; Hildebrandt, N.; Werts, M. H. V. Nanosurface Energy Transfer from Long-Lifetime Terbium

Donors to Gold Nanoparticles. *J. Phys. Chem. C* **2018**, *122* (30), 17566–17574.

(18) Chen, C.; Hildebrandt, N. Resonance energy transfer to gold nanoparticles: NSET defeats FRET. *TrAC, Trends Anal. Chem.* **2020**, *123*, 115748.

(19) Zhu, S.; Zhang, J.; Tang, S.; Qiao, C.; Wang, L.; Wang, H.; Liu, X.; Li, B.; Li, Y.; Yu, W.; Wang, X.; Sun, H.; Yang, B. Surface Chemistry Routes to Modulate the Photoluminescence of Graphene Quantum Dots: From Fluorescence Mechanism to Up-Conversion Bioimaging Applications. *Adv. Funct. Mater.* **2012**, *22* (22), 4732–4740.

(20) Zheng, X. T.; Ananthanarayanan, A.; Luo, K. Q.; Chen, P. Glowing Graphene Quantum Dots and Carbon Dots: Properties, Syntheses, and Biological Applications. *Small* **2015**, *11* (14), 1620–1636.

(21) Li, R. S.; Yuan, B.; Liu, J. H.; Liu, M. L.; Gao, P. F.; Li, Y. F.; Li, M.; Huang, C. Z. Boron and nitrogen co-doped single-layered graphene quantum dots: a high-affinity platform for visualizing the dynamic invasion of HIV DNA into living cells through fluorescence resonance energy transfer. *J. Mater. Chem. B* **2017**, *5* (44), 8719–8724.

(22) Kadian, S.; Manik, G.; Das, N.; Nehra, P.; Chauhan, R. P.; Roy, P. Synthesis, characterization and investigation of synergistic antibacterial activity and cell viability of silver–sulfur doped graphene quantum dot (Ag@S-GQDs) nanocomposites. *J. Mater. Chem. B* **2020**, *8* (15), 3028–3037.

(23) Zhu, C.; Yang, S.; Wang, G.; Mo, R.; He, P.; Sun, J.; Di, Z.; Yuan, N.; Ding, J.; Ding, G.; Xie, X. Negative induction effect of graphite N on graphene quantum dots: tunable band gap photoluminescence. *J. Mater. Chem. C* **2015**, *3* (34), 8810–8816.

(24) Huang, H.; Yang, S.; Liu, Y.; Yang, Y.; Li, H.; McLeod, J. A.; Ding, G.; Huang, J.; Kang, Z. Photocatalytic Polymerization from Amino Acid to Protein by Carbon Dots at Room Temperature. *ACS Applied Bio Materials* **2019**, *2* (11), 5144–5153.

(25) Kadian, S.; Manik, G.; Kalkal, A.; Singh, M.; Chauhan, R. P. Effect of sulfur doping on fluorescence and quantum yield of graphene quantum dots: an experimental and theoretical investigation. *Nanotechnology* **2019**, *30* (43), 435704.

(26) Zhu, J.; Tang, Y.; Wang, G.; Mao, J.; Liu, Z.; Sun, T.; Wang, M.; Chen, D.; Yang, Y.; Li, J.; Deng, Y.; Yang, S. Green, Rapid, and Universal Preparation Approach of Graphene Quantum Dots under Ultraviolet Irradiation. *ACS Appl. Mater. Interfaces* **2017**, *9* (16), 14470–14477.

(27) Qu, D.; Zheng, M.; Zhang, L.; Zhao, H.; Xie, Z.; Jing, X.; Haddad, R. E.; Fan, H.; Sun, Z. Formation mechanism and optimization of highly luminescent N-doped graphene quantum dots. *Sci. Rep.* **2015**, *4*, 5294.

(28) Qu, D.; Zheng, M.; Li, J.; Xie, Z.; Sun, Z. Tailoring color emissions from N-doped graphene quantum dots for bioimaging applications. *Light: Sci. Appl.* **2015**, *4*, e364.

(29) Liu, S.; Tian, J.; Wang, L.; Zhang, Y.; Qin, X.; Luo, Y.; Asiri, A. M.; Al-Youbi, A. O.; Sun, X. Hydrothermal Treatment of Grass: A Low-Cost, Green Route to Nitrogen-Doped, Carbon-Rich, Photoluminescent Polymer Nanodots as an Effective Fluorescent Sensing Platform for Label-Free Detection of Cu(II) Ions. *Adv. Mater.* **2012**, *24* (15), 2037–2041.

(30) Yang, S.; Sun, J.; Zhu, C.; He, P.; Peng, Z.; Ding, G. Supramolecular recognition control of polyethylene glycol modified N-doped graphene quantum dots: tunable selectivity for alkali and alkaline-earth metal ions. *Analyst* **2016**, *141* (3), 1052–1059.

(31) Li, J.; Yang, S.; Deng, Y.; Chai, P.; Yang, Y.; He, X.; Xie, X.; Kang, Z.; Ding, G.; Zhou, H.; Fan, X. Emancipating Target-Functionalized Carbon Dots from Autophagy Vesicles for a Novel Visualized Tumor Therapy. *Adv. Funct. Mater.* **2018**, *28* (30), 1800881.

(32) Vashist, S. K.; Lam, E.; Hrapovic, S.; Male, K. B.; Luong, J. H. T. Immobilization of Antibodies and Enzymes on 3-Aminopropyltriethoxysilane-Functionalized Bioanalytical Platforms for Biosensors and Diagnostics. *Chem. Rev.* **2014**, *114* (21), 11083–11130.

(33) Biju, V. Chemical modifications and bioconjugate reactions of nanomaterials for sensing, imaging, drug delivery and therapy. *Chem. Soc. Rev.* **2014**, *43* (3), 744–764.

(34) Xu, S.; Dong, B.; Zhou, D.; Yin, Z.; Cui, S.; Xu, W.; Chen, B.; Song, H. Paper-based upconversion fluorescence resonance energy transfer biosensor for sensitive detection of multiple cancer biomarkers. *Sci. Rep.* **2016**, *6*, 23406.

(35) Kumar, S.; Ashish; Kumar, S.; Augustine, S.; Yadav, S.; Yadav, B. K.; Chauhan, R. P.; Dewan, A. K.; Malhotra, B. D. Effect of Brownian motion on reduced agglomeration of nanostructured metal oxide towards development of efficient cancer biosensor. *Biosens. Bioelectron.* **2018**, *102*, 247–255.

(36) Mayilo, S.; Kloster, M. A.; Wunderlich, M.; Lutich, A.; Klar, T. A.; Nichtl, A.; Kürzinger, K.; Stefani, F. D.; Feldmann, J. Long-Range Fluorescence Quenching by Gold Nanoparticles in a Sandwich Immunoassay for Cardiac Troponin T. *Nano Lett.* **2009**, *9* (12), 4558–4563.

(37) Sidhu, J. S.; Singh, A.; Garg, N.; Kaur, N.; Singh, N. Gold conjugated carbon dots nano assembly: FRET paired fluorescence probe for cysteine recognition. *Sens. Actuators, B* **2019**, *282*, 515–522.

(38) Wu, Z. L.; Gao, M. X.; Wang, T. T.; Wan, X. Y.; Zheng, L. L.; Huang, C. Z. A general quantitative pH sensor developed with Dicyandiamide N-doped high quantum yield graphene quantum dots. *Nanoscale* **2014**, *6* (7), 3868–3874.

(39) Kuo, W.-S.; Shao, Y.-T.; Huang, K.-S.; Chou, T.-M.; Yang, C.-H. Antimicrobial Amino-Functionalized Nitrogen-Doped Graphene Quantum Dots for Eliminating Multidrug-Resistant Species in Dual-Modality Photodynamic Therapy and Bioimaging under Two-Photon Excitation. *ACS Appl. Mater. Interfaces* **2018**, *10* (17), 14438–14446.

(40) Sandeep Kumar, G.; Roy, R.; Sen, D.; Ghorai, U. K.; Thapa, R.; Mazumder, N.; Saha, S.; Chattopadhyay, K. K. Amino-functionalized graphene quantum dots: origin of tunable heterogeneous photoluminescence. *Nanoscale* **2014**, *6* (6), 3384–3391.

(41) Zheng, M.; Xie, Z.; Qu, D.; Li, D.; Du, P.; Jing, X.; Sun, Z. On–Off–On Fluorescent Carbon Dot Nanosensor for Recognition of Chromium(VI) and Ascorbic Acid Based on the Inner Filter Effect. *ACS Appl. Mater. Interfaces* **2013**, *5* (24), 13242–13247.

(42) Zhai, X.; Zhang, P.; Liu, C.; Bai, T.; Li, W.; Dai, L.; Liu, W. Highly luminescent carbon nanodots by microwave-assisted pyrolysis. *Chem. Commun.* **2012**, *48* (64), 7955–7957.

(43) *Material Studio*; Dassault Systemes BIOVIA: UK, 2020.

(44) Nair, R. R.; Debnath, S.; Das, S.; Wakchaure, P.; Ganguly, B.; Chatterjee, P. B. A Highly Selective Turn-On Biosensor for Measuring Spermine/Spermidine in Human Urine and Blood. *ACS Applied Bio Materials* **2019**, *2* (6), 2374–2387.

(45) Sukumar, U. K.; Packirisamy, G. Fabrication of Nanofibrous Scaffold Grafted with Gelatin Functionalized Polystyrene Microspheres for Manifesting Nanomechanical Cues of Stretch Stimulated Fibroblast. *ACS Applied Bio Materials* **2019**, *2* (12), 5323–5339.

(46) Ghosh, D.; Chattopadhyay, N. J. O. Gold nanoparticles: acceptors for efficient energy transfer from the photoexcited fluorophores. *Opt. Photonics J.* **2013**, *3* (1), 18–26.

(47) Ashish; Ahmad, N.; Gopinath, P.; Vinogradov, A.; Ahmad, N.; Gopinath, P.; Dutta, R. Chapter 1 - 3D Printing in Medicine: Current Challenges and Potential Applications. *3D Printing Technology in Nanomedicine* **2019**, 1–22.

(48) Augustine, S.; Kumar, P.; Malhotra, B. D. Amine-Functionalized MoO₃@RGO Nanohybrid-Based Biosensor for Breast Cancer Detection. *ACS Applied Bio Materials* **2019**, *2* (12), 5366–5378.

(49) Dorsey, M. P.; Nguelifack, B. M.; Yates, E. A. Colorimetric Detection of Mutant β -Amyloid(1–40) Membrane-Active Aggregation with Biosensing Vesicles. *ACS Applied Bio Materials* **2019**, *2* (11), 4966–4977.

(50) Yu, X.; Wang, Y.; Chen, X.; Wu, K.; Chen, D.; Ma, M.; Huang, Z.; Wu, W.; Li, C. White-Light-Exciting, Layer-by-Layer-Assembled ZnCdHgSe Quantum Dots/Polymerized Ionic Liquid Hybrid Film for Highly Sensitive Photoelectrochemical Immunosensing of Neuron Specific Enolase. *Anal. Chem.* **2015**, *87* (8), 4237–4244.

- (51) Zhong, Z.; Shan, J.; Zhang, Z.; Qing, Y.; Wang, D. The Signal-Enhanced Label-Free Immunosensor Based on Assembly of Prussian Blue-SiO₂ Nanocomposite for Amperometric Measurement of Neuron-Specific Enolase. *Electroanalysis* **2010**, *22* (21), 2569–2575.
- (52) Yu, T.; Cheng, W.; Li, Q.; Luo, C.; Yan, L.; Zhang, D.; Yin, Y.; Ding, S.; Ju, H. Electrochemical immunosensor for competitive detection of neuron specific enolase using functional carbon nanotubes and gold nanoprobe. *Talanta* **2012**, *93*, 433–438.
- (53) Han, J.; Zhuo, Y.; Chai, Y.-Q.; Yuan, Y.-L.; Yuan, R. Novel electrochemical catalysis as signal amplified strategy for label-free detection of neuron-specific enolase. *Biosens. Bioelectron.* **2012**, *31* (1), 399–405.
- (54) Li, H.; Cao, Z.; Zhang, Y.; Lau, C.; Lu, J. Simultaneous detection of two lung cancer biomarkers using dual-color fluorescence quantum dots. *Analyst* **2011**, *136* (7), 1399–1405.
- (55) Peng, J.; Feng, L.-N.; Zhang, K.; Li, X.-H.; Jiang, L.-P.; Zhu, J.-J. Calcium Carbonate–Gold Nanocluster Hybrid Spheres: Synthesis and Versatile Application in Immunoassays. *Chem. - Eur. J.* **2012**, *18* (17), 5261–5268.
- (56) Fu, X.; Meng, M.; Zhang, Y.; Yin, Y.; Zhang, X.; Xi, R. Chemiluminescence enzyme immunoassay using magnetic nanoparticles for detection of neuron specific enolase in human serum. *Anal. Chim. Acta* **2012**, *722*, 114–118.
- (57) Li, H.; Xiao, Q.; Lv, J.; Lei, Q.; Huang, Y. Dopamine modified hyperbranched TiO₂ arrays based ultrasensitive photoelectrochemical immunosensor for detecting neuron specific enolase. *Anal. Biochem.* **2017**, *531*, 48–55.
- (58) Fan, Y.; Liu, J.; Wang, Y.; Luo, J.; Xu, H.; Xu, S.; Cai, X. A wireless point-of-care testing system for the detection of neuron-specific enolase with microfluidic paper-based analytical devices. *Biosens. Bioelectron.* **2017**, *95*, 60–66.



Ti₃C₂-MXene decorated with nanostructured silver as a dual-energy acceptor for the fluorometric neuron specific enolase detection

Ashish Kalkal^a, Sachin Kadian^b, Sumit Kumar^c, Gaurav Manik^b, Prosenjit Sen^d, Saurabh Kumar^{d,e,**}, Gopinath Packirisamy^{a,f,*}

^a Nanobiotechnology Laboratory, Department of Biosciences and Bioengineering, Indian Institute of Technology Roorkee, Uttarakhand, 247667, India

^b Department of Polymer and Process Engineering, Indian Institute of Technology Roorkee, Uttarakhand, 247667, India

^c Department of Research and Innovations, Division of Research and Development, Lovely Professional University, Jalandhar, Punjab, 144411, India

^d Centre for Nano Science and Engineering (CeNSE), Indian Institute of Science Bengaluru, Karnataka, 560012, India

^e Department of Medical Devices, National Institute of Pharmaceutical Education and Research Guwahati, Assam, 781101, India

^f Centre for Nanotechnology, Indian Institute of Technology Roorkee, Uttarakhand, 247667, India

ARTICLE INFO

Keywords:

Energy transfer
Ti₃C₂-MXene
Graphene quantum dots (GQDs)
Fluorescent biosensor
Neuron-specific enolase (NSE)

ABSTRACT

Nanohybrids of two-dimensional (2D) layered materials have shown fascinating prospects towards the fabrication of highly efficient fluorescent immunosensor. In this context, a nanohybrid of ultrathin Ti₃C₂-MXene nanosheets and silver nanoparticles (Ag@Ti₃C₂-MXene) has been reported as a dual-energy acceptor for ultra-high fluorescence quenching of protein-functionalized graphene quantum dots (anti-NSE/amino-GQDs). The Ti₃C₂-MXene nanosheets are decorated with silver nanoparticles (AgNPs) to obsolete the agglomeration and restacking through a one-pot direct reduction method wherein the 2D Ti₃C₂-MXene nanosheets acted both as a reducing agent and support matrix for AgNPs. The as-prepared nanohybrid is characterized by various techniques to analyze the optical, structural, compositional, and morphological parameters. The quenching efficiency and energy transfer capability between the anti-NSE/amino-GQDs (donor) and Ag@Ti₃C₂-MXene (acceptor) have been explored through steady state and time-resolved spectroscopic studies. Interestingly, the Ag@Ti₃C₂-MXene nanohybrid exhibits better quenching and energy transfer efficiencies in contrast to bare Ti₃C₂-MXene, AgNPs and previously reported AuNPs. Based on optimized donor-acceptor pair, a fluorescent turn-on biosensing system is constructed that revealed improved biosensing characteristics compared to Ti₃C₂-MXene, graphene and AuNPs for the detection of neuron-specific enolase (NSE), including higher sensitivity (~771 mL ng⁻¹), broader linear detection range (0.0001–1500 ng mL⁻¹), better LOD (0.05 pg mL⁻¹), and faster response time (12 min). Besides, remarkable biosensing capability has been observed in serum samples, with fluorescence recovery of ~98%.

1. Introduction

A rapid accession in the exploration of zero-dimensional (0D) and two-dimensional (2D) based nanohybrid materials comprising derivatives of graphene, metal nanoparticles, transition metal oxides, dichalcogenides, including carbides, nitrides, and carbonitrides has shown a multifold rise in the field of bio and nanoelectronics engineering (Anasori et al., 2017; Chauhan et al., 2020; Kalkal et al., 2021c; Kumar et al. 2016, 2018a, Kumar et al., 2019a; Liu et al., 2017; Peng et al., 2016). These advanced materials possess exceptional optical,

mechanical, electronic, and physicochemical properties. Owing to these properties, their utilization has shown a well-proven scope in plenty of applications, especially energy conversion (Kumar et al., 2019b; Sun et al., 2017), supercapacitor (Zhou et al., 2020), biomedical (Huang et al., 2018), water purification (Pandey et al., 2018), and biosensing (Kumar et al., 2018a; Pradhan et al., 2021a). Moreover, in the last decade, 2D layered materials delivered an extraordinary impact in the field of fluorescent biosensors, wherein efficient donor-acceptor pairs are being explored to obtain enhanced energy transfer rates in view of achieving improved analytical performance (Neema et al., 2020; Peng

* Corresponding author. Nanobiotechnology Laboratory, Department of Biosciences and Bioengineering, Indian Institute of Technology Roorkee, Uttarakhand, 247667, India.

** Corresponding author. Centre for Nano Science and Engineering (CeNSE), Indian Institute of Science Bengaluru, Karnataka, 560012, India.

E-mail addresses: sau2203@gmail.com (S. Kumar), genegopi@gmail.com, gopi@bt.iitr.ac.in (G. Packirisamy).

<https://doi.org/10.1016/j.bios.2021.113620>

Received 27 May 2021; Received in revised form 18 August 2021; Accepted 6 September 2021

Available online 16 September 2021

0956-5663/© 2021 Elsevier B.V. All rights reserved.

et al., 2019; Tian et al., 2017; Zhu et al., 2019).

In this direction, quantum dots, including molybdenum disulfide (MoS_2), carbon dots (CDs), graphene quantum dots (GQDs), etc., have immensely evolved as energy donor species due to their unusual optical and electronic properties (Bhatnagar et al., 2016; Kadian et al., 2019; Kalkal et al., 2021a; Shao et al., 2019; Swaminathan et al., 2017). These quantum dots provide good biocompatibility, broad excitation spectra, good water solubility, tunable emission spectra, and intense fluorescence with long-term photostability (Kalkal et al., 2020, 2021b). On the other hand, 0D and 2D nanomaterials, including metal nanoparticles (gold and silver nanoparticles (Au and Ag NPs), graphene and its derivatives (reduced graphene oxide (RGO), graphene oxide (GO)) have been deployed as energy acceptor species in the development of fluorescent biosensors (Ghosh and Chattopadhyay, 2015; Neema et al., 2020). Conforming to this, Amjadi et al. demonstrated the fluorescent turn-on sensing probe for the detection of cysteine that utilizes CDs and AgNPs as donor-acceptor pair (Amjadi et al., 2015). In our previous work, we recently reported the development of a fluorescent biosensor for NSE detection based on AuNPs and amine-functionalized nitrogen-doped GQDs (Kalkal et al., 2020). Conversely, Bhatnagar et al. fabricated an immunosensor utilizing GQDs and graphene as energy donor-acceptor pair for detecting cardiac troponin I (CTnI) biomarker. (Bhatnagar et al., 2016).

However, it has been predicted that dispersed metal nanoparticles may tend to agglomerate in solution due to the Brownian motion of suspended nanoparticles, forming larger clusters having a smaller surface area that may inhibit the energy transfer efficiency and quenching capabilities (Mahdavi et al., 2019; Tilaki et al., 2006). Besides, 2D layered nanomaterials have a tendency to restack due to strong van der Waals forces between the adjacent nanosheets that may further influence the biosensing parameters (Atif and Inam, 2016; Cha et al., 2016; He et al., 2019). These problems might be overcome by preparing a 0D and 2D-based nanohybrid material that can work as a dual-energy acceptor and facilitate in improving the energy transfer efficiency along with biosensing parameters. In that, 2D layered nanomaterial can help in inhibiting the Brownian motion of metal nanoparticles by acting as a support matrix, thereby avoiding the inherent agglomeration. Additionally, the restacking among the 2D nanosheets can be inhibited by incorporating the 0D nanoparticles that help in generating the interlayer spacing among layered nanosheets (Kalali et al., 2020; Torres-Mendieta et al., 2016). In this context, Kumar et al. utilized the RGO nanosheets as the support matrix to reduce the agglomeration by inhibiting the Brownian motion of nanostructured metal oxide. The resultant nanohybrid-based sensing platform exhibited superior biosensing parameters, including higher sensitivity and broader linear detection range (Kumar et al., 2018a; Kumar and Kalkal, 2021). However, in case of graphene-based 2D nanomaterials, the decoration of 0D nanomaterials can occur only on edge and defect sites of graphene nanosheets (Bellunato et al., 2016; Vedala et al., 2011). Besides, chemically synthesized graphene (RGO) requires an additional reducing agent for *in-situ* decoration or an additional step for *ex-situ* decoration of 0D nanomaterial on RGO nanosheets (Cui et al., 2013; Ikram et al., 2020; Su et al., 2018). Moreover, the conventional graphene-based 2D layered nanomaterials possess low-hydrophilicity, inadequate surface terminated functionality, difficulty in functionalization that may influence the intrinsic properties and fluorescent biosensing applications of graphene-based layered materials.

In the view of foregoing, a new and emerging material named MXene having the general formula of $\text{M}_{n+1}\text{X}_n\text{T}_x$ (M represents a transition metal, X can be nitrogen and/or carbon, and T_x denotes surface functionalization) has attracted enormous consideration for the biosensing applications (Ghidiu et al., 2014; Khazaei et al., 2013; Naguib et al., 2011). Among them, Ti_3C_2 -MXene is known for its metallic conductivity, super hydrophilicity, broad and strong absorption, polar surfaces, large surface area, which make them viable for electrochemical as well as fluorescent biosensors (Anasori et al., 2017; Kumar et al., 2018b;

Zhang et al., 2018). The ultrathin Ti_3C_2 -MXene sheets terminated with oxygen and hydroxyl groups facilitate the material to communicate with a large number of biomolecules via hydrogen bonds, coordination bonds, van der Waals forces, and electrostatic interactions. Moreover, Ti_3C_2 -MXene sheets exhibit wideband absorption in UV–vis region over its large surface area in conjunction with long-range electron and energy transferability, which enable the Ti_3C_2 -MXene to become a prominent energy acceptor or quencher species (Shi et al., 2019; Zhang et al., 2018). Despite great potential, it has been observed that Ti_3C_2 -MXene as a fluorescence quencher/energy acceptor is not explored much, and only a few attempts have been made in this direction (Peng et al., 2019; Shi et al., 2019; Zhang et al., 2018; Zhu et al., 2019). Unlike graphene, Ti_3C_2 -MXene offers excellent aqueous solubility, superior surface terminated functionality, larger surface area, and better biocompatibility, preferable in the fabrication of efficient fluorescent biosensors (Song et al., 2020; Soomro et al., 2020). Besides, the self-reducing capability of Ti_3C_2 -MXene exempt the requirement of additional reducing agent for decorating 0D nanomaterial on Ti_3C_2 -MXene nanosheets.

Small cell lung cancer (SCLC) a distinct histological subgroup of lung cancer, is associated with poor prognosis, strong predilection for early metastasis, and exceptionally high proliferative rate (Rudin et al., 2021). SCLC is the most hostile form of lung cancer, accounting for around 15–20% of new cases. Besides, it is marked by acquired chemoresistance and high sensitivity to radiation and chemotherapy, and therefore difficult to cure (Jackman and Johnson, 2005). It can be life-threatening and metastasize to other body parts if not diagnosed at an initial stage. Therefore, there is an increased demand for SCLC's rapid and early detection, lowering the mortality rate. In this context, neuron specific enolase (NSE) is reported as an efficient biomarker for monitoring therapeutic treatment efficacy, disease progression, assessing tumor burden, and early diagnosis in view of its higher secretion rate (Amani et al., 2018; Han et al., 2012; Xiao et al., 2017). For healthy persons, the NSE concentration in serum can be up to 12–13 ng mL^{-1} while SCLC patients have this concentration more than 35 ng mL^{-1} (Harding et al., 1990; Kalkal et al., 2020; Shibayama et al., 2001). Quantitative detection of NSE in serum can be an exciting alternative for monitoring and clinical diagnosis of SCLC.

We report results of the studies relating to the fabrication and utilization of $\text{Ag}@\text{Ti}_3\text{C}_2$ -MXene nanohybrid as a dual-energy acceptor for the development of a rapid, label-free, and highly sensitive fluorescent biosensor. The fabricated biosensor rely on the efficient trade-off between the donor (anti-NSE/amino-GQDs) and acceptor ($\text{Ag}@\text{Ti}_3\text{C}_2$ -MXene) pair following the nanosurface energy transfer (NSET) mechanism. The $\text{Ag}@\text{Ti}_3\text{C}_2$ -MXene nanohybrid based biosensor reveals improved biosensing characteristics in standard and spiked serum samples for NSE detection compared to bare Ti_3C_2 -MXene, classic graphene and earlier reported AuNPs (Kalkal et al., 2020).

2. Materials and methods

2.1. Preparation of $\text{Ag}@\text{Ti}_3\text{C}_2$ -MXene nanohybrid

$\text{Ag}@\text{Ti}_3\text{C}_2$ -MXene nanohybrid has been obtained via the one-pot direct reduction of aqueous AgNO_3 salt to AgNPs onto Ti_3C_2 -MXene nanosheets. In this process, the 2D Ti_3C_2 -MXene nanosheets acted both as a reducing agent and support matrix for AgNPs. Initially, 84.93 mg of AgNO_3 is dispersed in 50 mL of deionized water through a vortex mixture to provide the 10 mM aqueous solution. On the other hand, 200 mg of powdered Ti_3C_2 -MXene (supporting information, S3) is suspended in 20 mL of distilled water followed by ultrasonication for 30 min to provide the uniformly dispersed stock concentration (10 mg mL^{-1}). After that, 5 mL of dispersed Ti_3C_2 -MXene with diluted concentrations (0.5, 1, 2, 5 mg mL^{-1}) is added in a dropwise manner to the above-prepared AgNO_3 aqueous solution and continued stirring for 60 min. Fig. S1 shows the images of obtained $\text{Ag}@\text{Ti}_3\text{C}_2$ -MXene nanohybrid

solution with different $\text{Ti}_3\text{C}_2\text{-MXene}$ concentrations. The obtained solution of $\text{Ag@Ti}_3\text{C}_2\text{-MXene}$ nanohybrid is centrifuged at 10,000 rpm and washed multiple times to remove the impurities. Finally, the resultant solution is vacuum dried to obtain the powdered $\text{Ag@Ti}_3\text{C}_2\text{-MXene}$ nanohybrid.

2.2. Protein functionalization of amino graphene quantum dots (anti-NSE/amino-GQDs)

The hydrothermally synthesized amino-GQDs (supporting information, S4) are protein functionalized using the standard EDC-NHS coupling chemistry (Kalkal et al., 2020; Kumar et al., 2018a). To activate the carboxyl groups of monoclonal anti-NSE antibody, a solution containing 250 μL of anti-NSE ($50 \mu\text{g mL}^{-1}$), 125 μL of NHS (0.05 M), and 125 μL of EDC (0.2 M) is prepared and allowed to incubate for 30 min at room temperature. The activated anti-NSE antibody solution is mixed with an equal volume (500 μL , 1:1 v/v) of amino-GQDs solution ($20 \mu\text{g mL}^{-1}$) and incubated in a humid chamber for about 2 h. After that, the anti-NSE/amino-GQDs solution is ultra-centrifuged and washed with deionized water to remove the unbound antibodies. The protein functionalized GQDs are characterized by zeta potential, FTIR, and UV-vis techniques (supporting information (S6), Figs. S2c–e).

2.3. Design of fluorescent biosensor

The detection of target cancer biomarker is carried out in 50 mM phosphate-buffered saline (PBS) solution (pH 7.4) at room temperature by recording the fluorescence emission spectra. Here, 500 μL of protein-functionalized amino-GQDs energy donor is mixed with 200 μL of $\text{Ag@Ti}_3\text{C}_2\text{-MXene}$ nanohybrid ($50 \mu\text{g mL}^{-1}$) energy acceptor. After that, 50 μL of distinct NSE concentrations ($0.0001\text{--}1500 \text{ ng mL}^{-1}$) is added to the donor-acceptor mixture (anti-NSE/amino-GQDs/ $\text{Ag@Ti}_3\text{C}_2\text{-MXene}$) and allowed to incubate for an interval of 12 min. Consequently, the

alterations in fluorescence intensity are computed at the excitation wavelength of 360 nm with the increasing NSE antigen concentration in the resultant mixture. The selectivity studies of the fabricated biosensor have been performed by adding fixed concentration (50 μL , 0.1 ng mL^{-1}) of various interfering biomarkers into anti-NSE/amino-GQDs/ $\text{Ag@Ti}_3\text{C}_2\text{-MXene}$ solution, followed by the measurement of corresponding emission spectra. The real sample analysis is performed in NSE spiked serum samples that are obtained from the hospital, Indian Institute of Technology Roorkee (IITR), after ethical approval by the Institutional Biosafety and Ethical Committee (BT/IHEC-IITR/2019/7525) (Pradhan et al., 2021b). 50 μL of serum samples spiked with different NSE concentrations (10, 20, 50, 100, and 150 ng mL^{-1}) is added into the optimized donor-acceptor solution (anti-NSE/amino-GQDs/ $\text{Ag@Ti}_3\text{C}_2\text{-MXene}$) to record the corresponding emission spectra as described above.

3. Results and discussion

3.1. Mechanism of proposed fluorescent biosensor

The working of the proposed anti-NSE/amino-GQDs/ $\text{Ag@Ti}_3\text{C}_2\text{-MXene}$ biosensor is elaborated in a three-step process, and a schematic representation of the plausible mechanism is illustrated in Fig. 1. The driving force behind any fluorescent biosensor is based on the fluorescent state (ON/OFF) of the fluorophore, irrespective of its nature. In the first step, the fluorescence intensity of synthesized donor species (anti-NSE/amino-GQDs) is recorded at an excitation wavelength of 360 nm, which emit intense blue fluorescence around 450 nm (ON state). Secondly, the optimized amount of anti-NSE/amino-GQDs are physically adsorbed on the surface of $\text{Ag@Ti}_3\text{C}_2\text{-MXene}$ nanohybrid through non-covalent interactions, which leads to an abrupt fluorescence quenching owing to dipole-surface interactions (OFF state). The $\text{Ag@Ti}_3\text{C}_2\text{-MXene}$ nanohybrid acts as a dual-quencher in a single system for ultra-

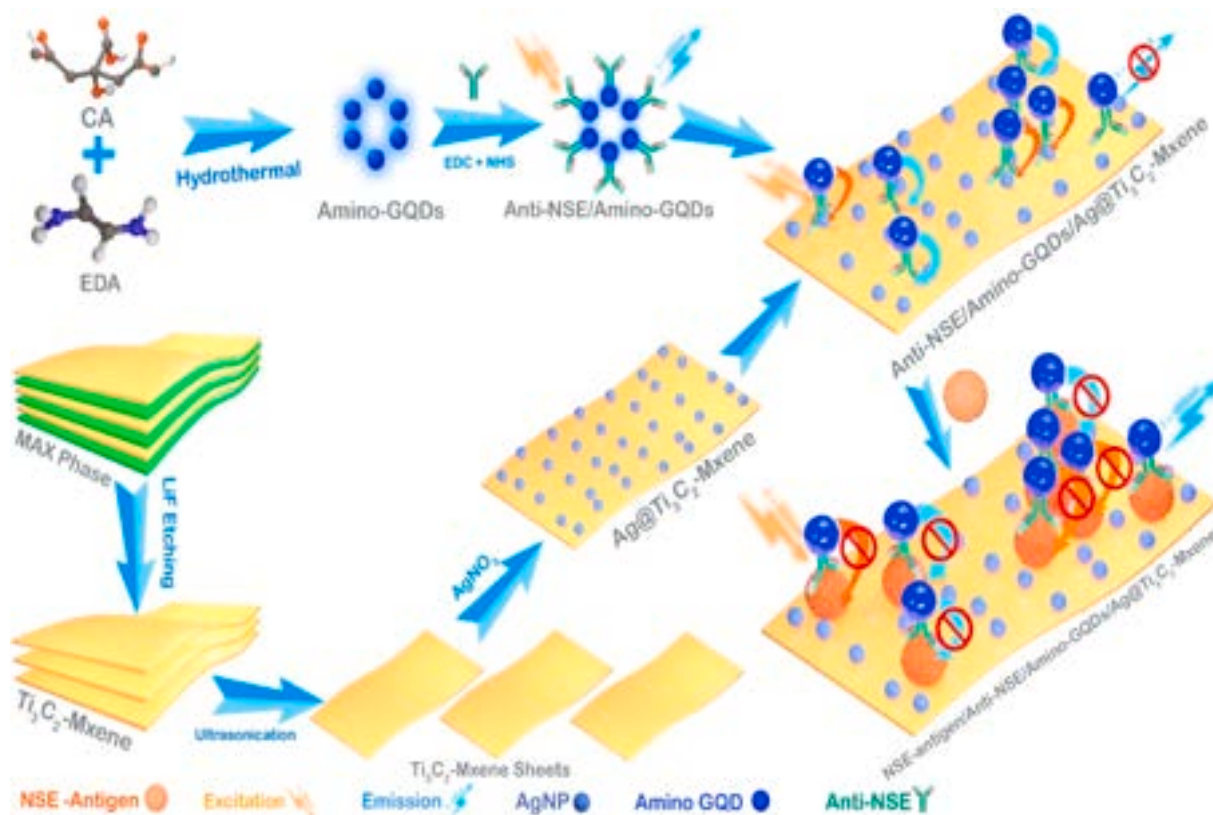


Fig. 1. Schematic illustration of anti-NSE/amino-GQDs/ $\text{Ag@Ti}_3\text{C}_2\text{-MXene}$ based biosensing platform for the fluorometric NSE detection.

high fluorescence quenching of donor species owing to their higher surface to volume ratio that enables effective energy transfer utilizing the concept of single-acceptor multiple-donor. In this context, the orange-colored arrows in Fig. 1 indicate the energy transfer to AgNPs from anti-NSE/amino-GQDs donor species. In contrast, energy transfer to $\text{Ti}_3\text{C}_2\text{-MXene}$ nanosheets is shown with cyan-colored arrows. The 0D-2D complex of $\text{Ag@Ti}_3\text{C}_2\text{-MXene}$ nanohybrid combines the benefit of both 0D AgNPs and 2D $\text{Ti}_3\text{C}_2\text{-MXene}$ as individual energy acceptors. At last, the addition of the target antigen in the anti-NSE/amino-GQDs/ $\text{Ag@Ti}_3\text{C}_2\text{-MXene}$ biocomplex leads to specific immunocomplex (antigen-antibody) formation. Due to this, the fluorescence gets recovered (ON state) from the non-interacted anti-NSE/amino-GQDs donor as they detached from the $\text{Ag@Ti}_3\text{C}_2\text{-MXene}$ nanohybrid surface due to the inferior non-covalent interactions. The recovered fluorescence from the donor species further relies on the added NSE concentration.

3.2. Characterizations of $\text{Ag@Ti}_3\text{C}_2\text{-MXene}$ nanohybrid

3.2.1. Optical characterizations

The optical properties of synthesized $\text{Ti}_3\text{C}_2\text{-MXene}$ and $\text{Ag@Ti}_3\text{C}_2\text{-MXene}$ nanohybrid are identified from their corresponding colloidal solutions. The color of the synthesized $\text{Ag@Ti}_3\text{C}_2\text{-MXene}$ nanohybrid complex appeared dark golden due to the reduction of AgNO_3 to AgNPs by $\text{Ti}_3\text{C}_2\text{-MXene}$ nanosheets (Fig. S1). Besides, the validation of

reduction has been studied through UV-vis spectroscopy (Fig. 2a), wherein initially a sharp absorption peak around 300 nm for AgNO_3 salt and a broad peak around 270 nm for $\text{Ti}_3\text{C}_2\text{-MXene}$ is observed (Kumar et al., 2018b). A continuous decrement in AgNO_3 peak intensity and subsequently an increment in the intensity of AgNPs surface plasmon resonance (SPR) peak at 438 nm, with increasing concentrations of $\text{Ti}_3\text{C}_2\text{-MXene}$ reflect the reduction and successful formation of $\text{Ag@Ti}_3\text{C}_2\text{-MXene}$ nanohybrid (Pandey et al., 2018).

3.2.2. Structural and morphological characterizations

The structural characterizations of synthesized AgNPs, $\text{Ti}_3\text{C}_2\text{-MXene}$ and $\text{Ag@Ti}_3\text{C}_2\text{-MXene}$ nanohybrid are investigated via XRD analysis (Fig. 2b). The AgNPs exhibits four sharp crystalline peaks associated to (111), (200), (220), and (311) planes at 2θ angle 38.5° , 44.7° , 64.8° , and 77.7° , respectively (JCPDS card no. 040783) (Zou et al., 2016). In $\text{Ti}_3\text{C}_2\text{-MXene}$, a weak and broad peak at $2\theta = 6.8$ corresponding to (002) plane is observed, elucidating the formation of $\text{Ti}_3\text{C}_2\text{-MXene}$ nanosheets (Kumar et al., 2018b). The spectrum of $\text{Ag@Ti}_3\text{C}_2\text{-MXene}$ replicates the diffraction peaks of AgNPs and $\text{Ti}_3\text{C}_2\text{-MXene}$, indicating the nanohybrid formation. Interestingly, no peak shift has been observed in the spectrum of resultant nanohybrid that evince the decoration of AgNPs on the surface of $\text{Ti}_3\text{C}_2\text{-MXene}$ nanosheets (Pandey et al., 2018).

The pivotal information such as surface chemical bonding, elemental composition, and the plausible direct reduction mechanism concerning

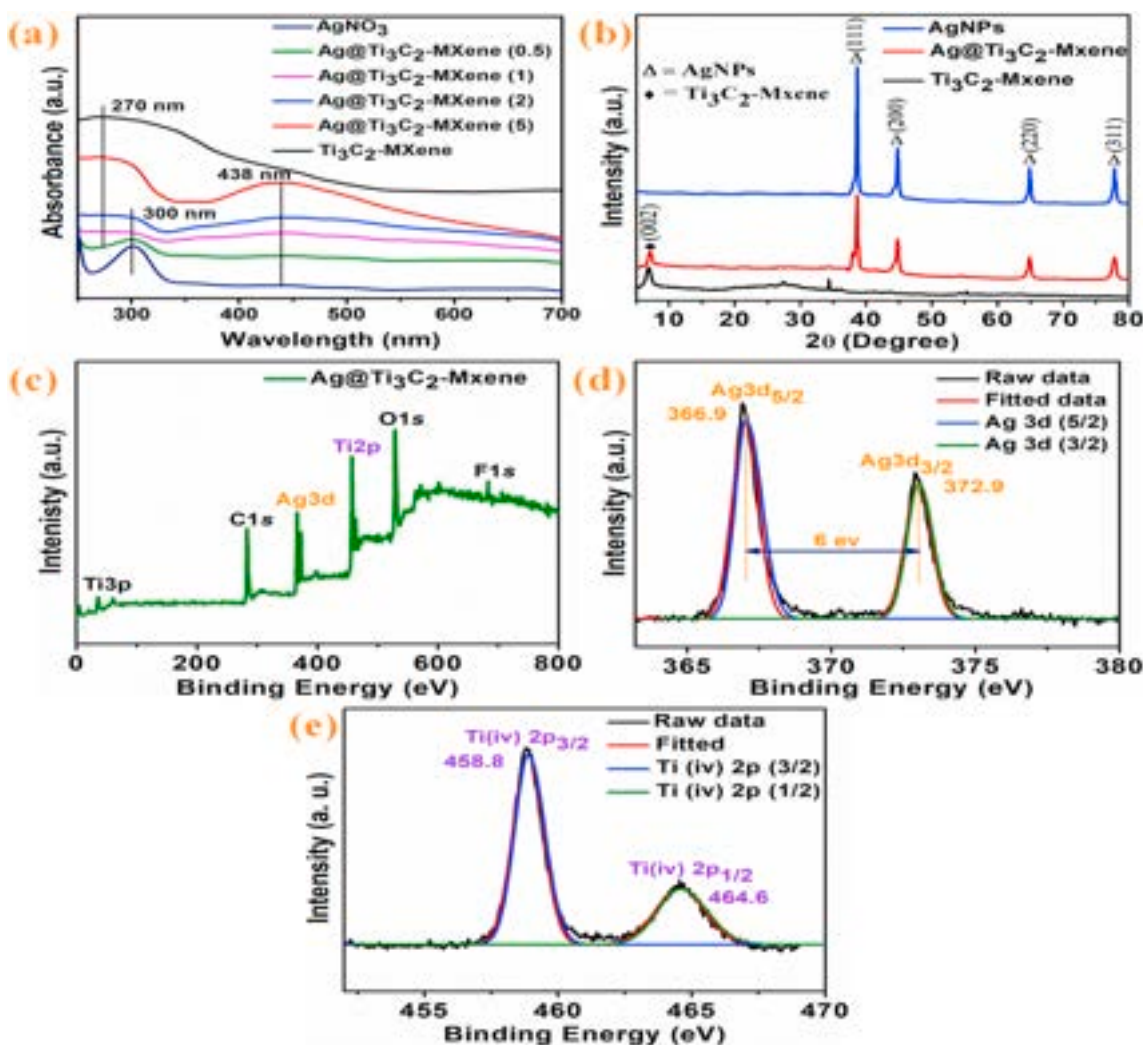


Fig. 2. (a) UV-vis absorption spectra of $\text{Ti}_3\text{C}_2\text{-MXene}$, $\text{Ag@Ti}_3\text{C}_2\text{-MXene}$ nanohybrid with different concentrations of $\text{Ti}_3\text{C}_2\text{-MXene}$ (0.5, 1, 2, 5 mg mL^{-1}), and AgNO_3 salt respectively; (b) Diffraction pattern of AgNPs, $\text{Ag@Ti}_3\text{C}_2\text{-MXene}$ nanohybrid, bare $\text{Ti}_3\text{C}_2\text{-MXene}$; (c) Full scan XPS profile of $\text{Ag@Ti}_3\text{C}_2\text{-MXene}$ nanohybrid; (d) Deconvoluted Ag 3d spectra for $\text{Ag@Ti}_3\text{C}_2\text{-MXene}$ nanohybrid; (e) Deconvoluted Ti 2p spectra for $\text{Ag@Ti}_3\text{C}_2\text{-MXene}$ nanohybrid.

Ag@Ti₃C₂-MXene nanohybrid are investigated through XPS analysis. The full scan XPS spectra of the synthesized Ag@Ti₃C₂-MXene nanohybrid reveal the existence of C 1s, Ag 3d, O 1s, Ti 2p, Ti 3p, and F1s components (Fig. 2c). The detailed chemical bonding analysis of Ag and Ti have been elucidated by deconvoluting the Ag 3d and Ti 2p spectra. The deconvoluted Ag 3d spectra (Fig. 2d) comprises two prominent peaks related to Ag 3d_{3/2} and Ag 3d_{5/2} at the binding energy of 372.9, 366.9 eV, respectively, indicating the direct reduction of silver from Ag⁺ to Ag(0) (Pandey et al., 2018). Additionally, the binding energy splitting is obtained 6 eV, demonstrating the presence of metallic AgNPs in the nanohybrid. Similarly, the deconvoluted Ti 2p spectra (Fig. 2e) comprises two main peaks at 458.8 and 464.6 eV related to Ti(iv) 2p_{3/2}, and Ti(iv) 2p_{1/2}, respectively (Zou et al., 2016). The self-reduction process provides the transformation of Ti (iii) and Ti (ii) to the terminated Ti (iv) species (Fig. 2e), validating the successful reduction of AgNO₃ to AgNPs by MXene nanosheets. This uniform deposition and self-reduction of AgNPs on Ti₃C₂-MXene nanosheets can be attributed to the activated low valence Ti species in the Ti₃C₂-MXene nanosheets (Pandey et al., 2018).

The detailed surface morphological analysis of synthesized Ti₃C₂-MXene and Ag@Ti₃C₂-MXene nanohybrid are investigated through TEM and FE-SEM characterizations. Stacked MXene flakes having flake sizes around 2–3 μm can be observed in the synthesized bare Ti₃C₂-MXene (Figs. S5–7). However, the Ag@Ti₃C₂-MXene nanohybrid indicates the

presence of non-aggregated and uniformly decorated AgNPs on ultrathin Ti₃C₂-MXene nanosheets (Fig. 3a–f). The energy dispersive X-ray spectroscopy (EDS) is also performed for the elemental spectrum, and mapping analysis. The EDS spectrum of Ti₃C₂-MXene (Fig. S3a) exhibits the occurrence of oxygen (O), carbon (C), and titanium (Ti) elements, whereas the spectrum of Ag@Ti₃C₂-MXene nanohybrid (Fig. S3b) reveals the existence of Ag along with O, C, and Ti. These elements are mapped with individual colors viz. yellow (Ag), turquoise (Ti), red (C), and green (O) for Ag@Ti₃C₂-MXene nanohybrid (Fig. 3h); and yellow (Ti), red (C), and green (O) for Ti₃C₂-MXene nanosheets (Fig. S4). Additionally, the line scan analysis is also carried out across the individual sheets, and their corresponding effects are depicted in Fig. S5 and Fig. 3i, which also evident the existence and distribution of these elements.

3.3. Steady-state and time-resolved spectroscopic studies between anti-NSE/amino-GQDs and Ag@Ti₃C₂-MXene nanohybrid

An effective energy transfer system requires an extensive selection of donor-acceptor pair that relies on the criteria of overlap between the emission spectra of donor species and absorption spectra of acceptor species (Neema et al., 2020). Herein, an optimal overlap has been obtained for the selected donor-acceptor pair, indicating the plausible energy transfer process (Fig. S8). Compared to previously reported

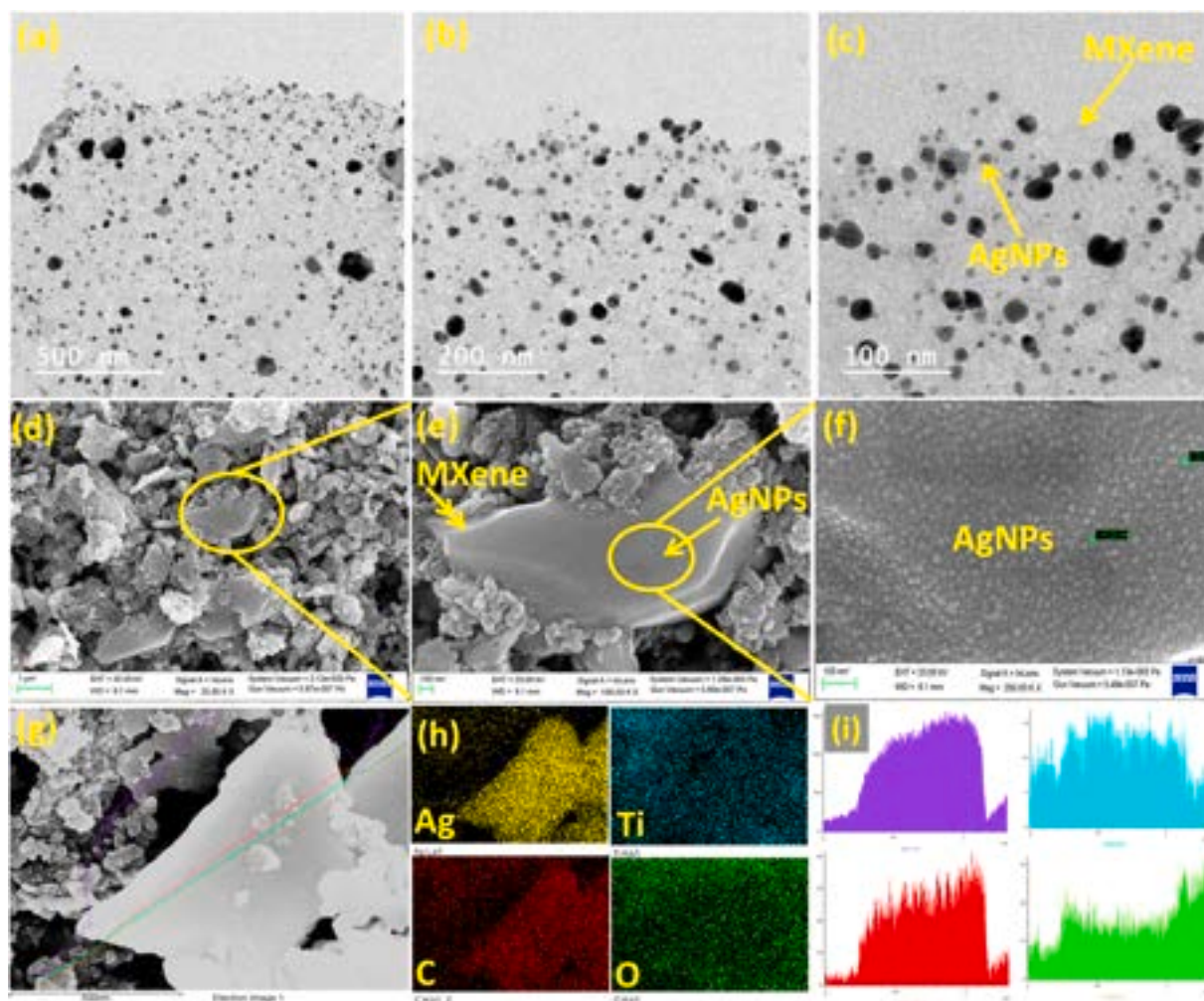


Fig. 3. (a–c) TEM images of Ag@Ti₃C₂-MXene nanohybrid at different scales, indicating the decoration of AgNPs on ultrathin Ti₃C₂-MXene nanosheets (d–g) FE-SEM images of Ag@Ti₃C₂-MXene nanohybrid at different magnifications; (h) Elemental mapping of Ag@Ti₃C₂-MXene revealing the presence of Ag (yellow), Ti (turquoise), C (red), and O (green) elements; (i) Line scan analysis of Ag@Ti₃C₂-MXene nanohybrid across the individual sheet. (For interpretation of the references to color in this figure legend, the reader is referred to the Web version of this article.)

AuNPs energy acceptor (Kalkal et al., 2020), the Ag@Ti₃C₂-MXene nanohybrid indicates better spectra overlap, signifying the improved energy transfer kinetics. The fluorescence quenching ability of Ag@Ti₃C₂-MXene nanohybrid has been compared with bare Ti₃C₂-MXene, AgNPs and earlier reported AuNPs. The protein-functionalized amino-GQDs are incubated with increasing concentrations of AgNPs, Ti₃C₂-MXene and Ag@Ti₃C₂-MXene nanohybrid followed by recording their corresponding emission spectra. It has been found that the fluorescence intensity of protein functionalized amino-GQDs decreases progressively after the addition of increasing concentrations of AgNPs (Fig. S9), Ti₃C₂-MXene (Fig. 4a), and Ag@Ti₃C₂-MXene (Fig. 4b) nanohybrid. This quenching can be attributed to the dipole-surface interactions between donor-acceptor pairs. The quenching efficiency (QE) with these materials was determined using Eq. (S1) and then compared. It has been observed that the Ag@Ti₃C₂-MXene exhibits higher quenching efficiency (~94%) compared to bare Ti₃C₂-MXene (~87%), AgNPs (~84) and AuNPs (~81%) (Kalkal et al., 2020). This increase in QE might be attributed to the synergistic effect of Ag@Ti₃C₂-MXene nanohybrid, which acts as a dual-quencher in a single system for the ultra-high fluorescence quenching of anti-NSE/amino-GQDs. The higher

surface to volume ratio of Ag@Ti₃C₂-MXene nanohybrid may enable efficient fluorescence quenching by introducing the concept of single-acceptor and multiple-donor (as depicted in Fig. 1). The integration of AgNPs to Ti₃C₂-MXene nanosheets offered a stable nanohybrid that may prevent the aggregation and stacking of bare AgNPs and Ti₃C₂-MXene nanosheets, respectively, resulting in enhanced QE.

Subsequently, the Stern-Volmer studies are examined to determine the quenching mechanism (Kumar et al., 2019a, 2020). In this context, Fig. 4d indicates the plots of F_0/F as a function of quencher concentration. The obtained linear plots signify the dynamic nature of quenching with both Ti₃C₂-MXene and Ag@Ti₃C₂-MXene (Swaminathan et al., 2017). Besides, the time-resolved fluorescence spectroscopy is carried out to study the nature of interactive energy transfer between donor-acceptor pair and measure the fluorescence lifetime of the donor in the presence and absence of quencher. Fig. 4e indicates the corresponding spectra of protein functionalized amino-GQDs with increasing Ag@Ti₃C₂-MXene concentrations. After the addition of increased Ag@Ti₃C₂-MXene concentration, the fluorescence lifetime of anti-NSE/amino-GQDs is observed to be progressively reduced, confirming the energy transfer mechanism from the anti-NSE/amino-GQDs

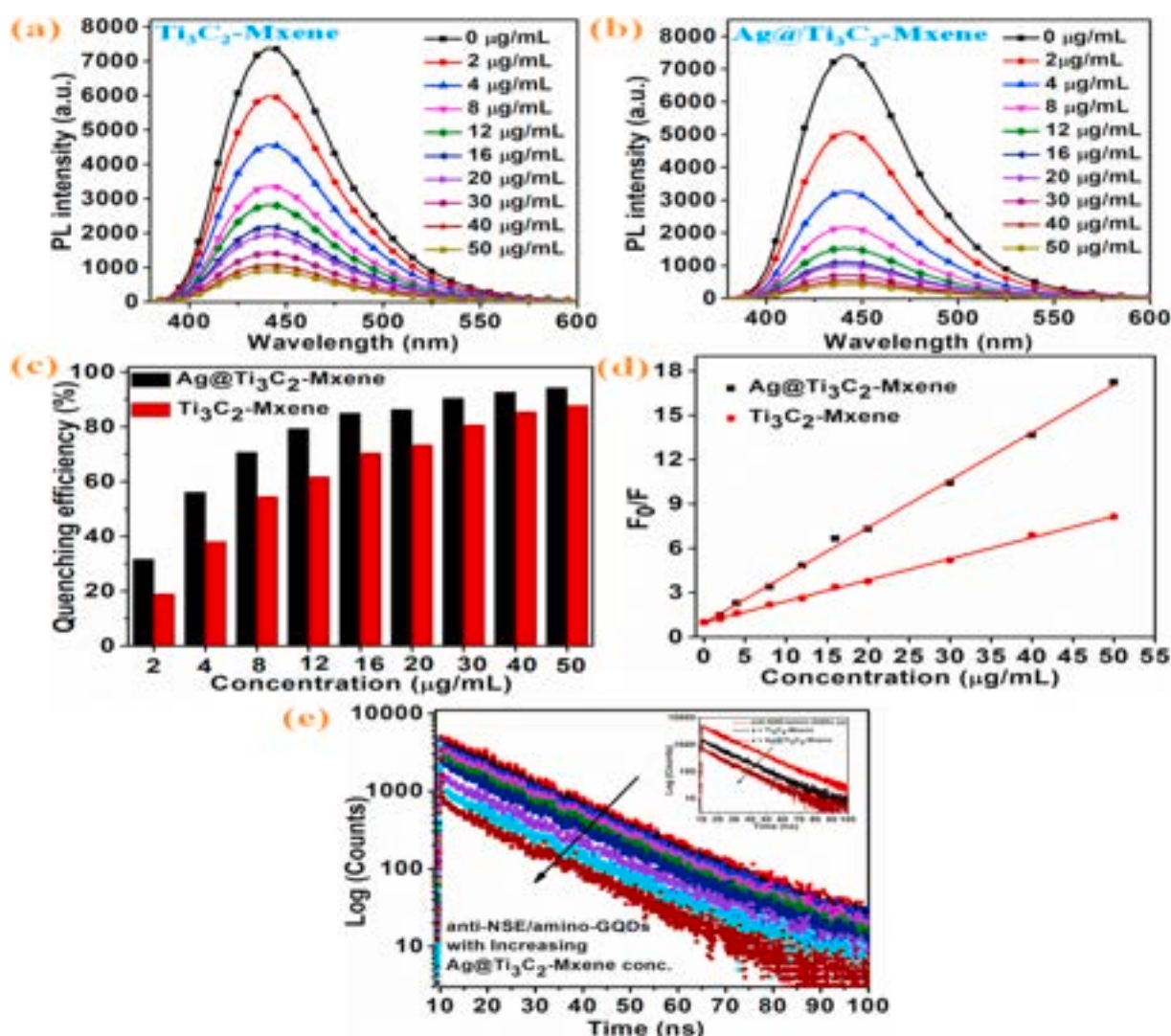


Fig. 4. Steady-state fluorescence quenching spectra of protein functionalized amino-GQDs with escalating concentrations (0–50 μg mL⁻¹ from top to bottom, λ_{ex} = 360 nm, λ_{em} ~ 450 nm); (a) bare Ti₃C₂-MXene (b) Ag@Ti₃C₂-MXene; (c) The comparison of fluorescence QE induced by Ti₃C₂-MXene and Ag@Ti₃C₂-MXene; (d) Stern-Volmer plot indicating the variation of F_0/F with different concentration of Ti₃C₂-MXene/Ag@Ti₃C₂-MXene from 0 to 50 μg mL⁻¹; (e) Time-resolved fluorescence spectra of protein-functionalized amino-GQDs with increasing concentration of Ag@Ti₃C₂-MXene nanohybrid (inset shows the lifetime decay spectra of protein-functionalized amino-GQDs alone and with added Ti₃C₂-MXene and Ag@Ti₃C₂-MXene (200 μL, 0.05 mg mL⁻¹).

to Ag@Ti₃C₂-MXene. In Fig. 4e, the downward inclined arrow states that the dynamics of emission decay become faster when the concentration of Ag@Ti₃C₂-MXene nanohybrid is increased. The protein functionalized amino-GQDs fluorescence lifetime follows bi-exponential decay dynamics with $\tau_1 = 8.04$ ns (fast component), and $\tau_2 = 16.64$ ns (slow component). Upon the addition of Ag@Ti₃C₂-MXene, the τ_1 , τ_2 decrease from 8.04 to 2.4 ns and 16.64 to 15.26 ns, respectively. The inset of Fig. 4e indicates the lifetime decay spectra of protein-functionalized amino-GQDs alone and added Ti₃C₂-MXene and Ag@Ti₃C₂-MXene (200 μ L, 0.05 mg mL⁻¹). The energy transfer performance of Ag@Ti₃C₂-MXene nanohybrid has been compared with bare Ti₃C₂-MXene and AuNPs (Kalkal et al., 2020), calculated using Eq. (1).

$$\varphi_E = 1 - \frac{\tau_{DA}}{\tau_D} \quad (1)$$

Where τ_{DA} and τ_D are the fluorescence lifetime of protein-functionalized amino-GQDs with and without quencher, respectively. It has been observed that the Ag@Ti₃C₂-MXene exhibits a higher energy transfer efficiency (~70%) compared to bare Ti₃C₂-MXene (~54) and AuNPs (43%) (Kalkal et al., 2020). This increased efficiency can be attributed to the prepared non-aggregated, unstaked, and stable Ag@Ti₃C₂-MXene

nanohybrid that might enable faster energy transfer kinetics from the donor species by working as an efficient dual-energy acceptor. The free conduction electrons present in AgNPs can facilitate in providing higher energy accepting capability through dipole vectors on their surface, high molecular extinction coefficient, and larger absorption spectra overlap near the Plasmon resonance frequency (Ghosh and Chattopadhyay, 2015). Furthermore, it is reported that AgNPs lack a defined dipole moment; thereby, energy transfer to AgNPs can occur in any orientation of donor species (Ghosh and Chattopadhyay, 2015; Shi et al., 2015). Apart from that, Ti₃C₂-MXene sheets exhibit wideband absorption in the UV-vis region over its large surface area in conjunction with long-range electron and energy transferability, providing improved energy transfer (Shi et al., 2019; Zhang et al., 2018).

3.4. Analytical performance of the anti-NSE/amino-GQDs/Ag@Ti₃C₂-MXene based fluorescent biosensor

Under optimal conditions (supporting information (S7), Figs. S10–S11), the fluorescence spectroscopy has been carried out to explore the analytical performance of anti-NSE/amino-GQDs/Ag@Ti₃C₂-MXene (Fig. 5a) and anti-NSE/amino-GQDs/Ti₃C₂-MXene

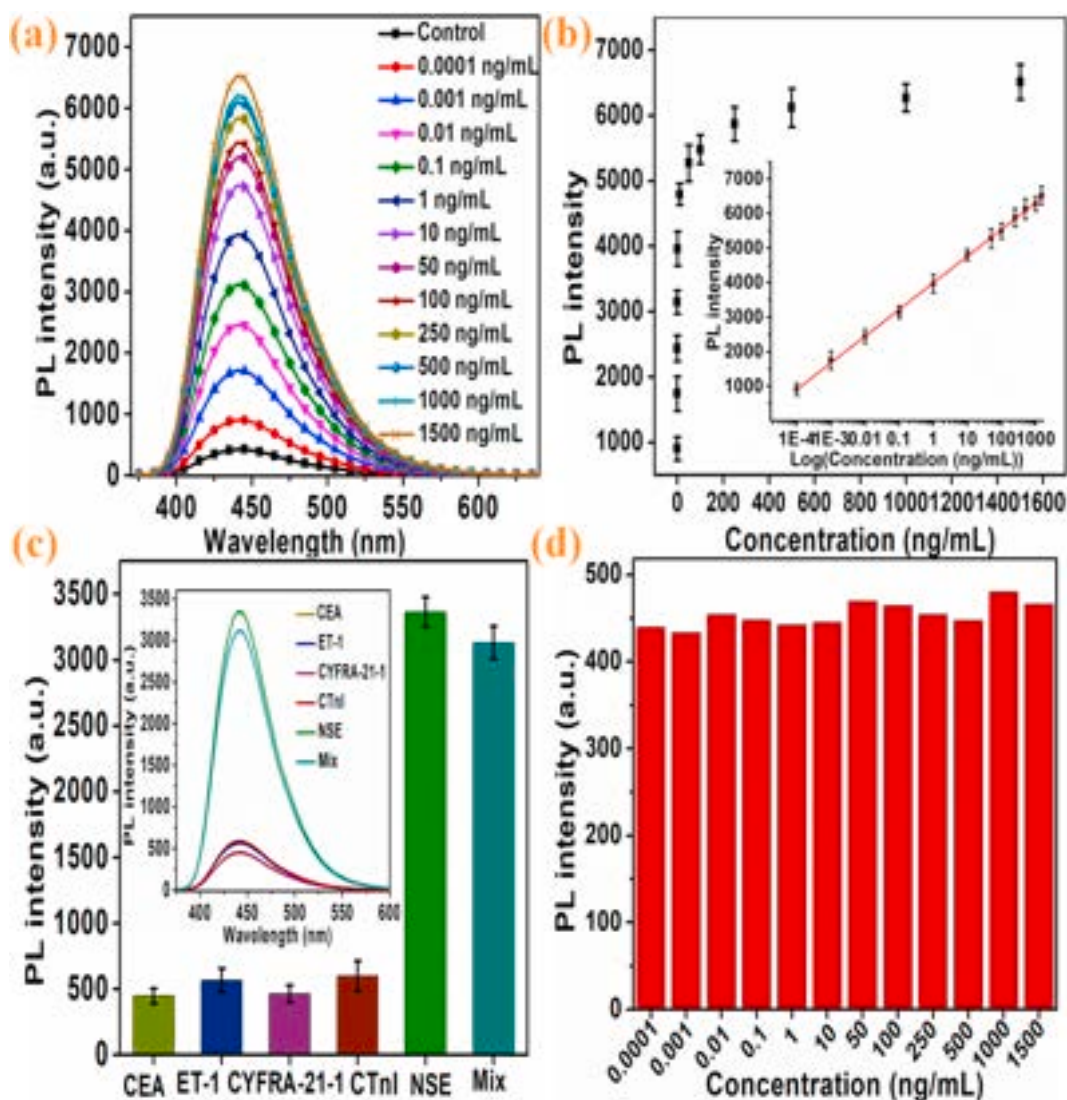


Fig. 5. (a) Analytical performance of the anti-NSE/amino-GQDs/Ag@Ti₃C₂-MXene based fluorescent biosensor toward NSE detection (b) Graph between recovered fluorescence and different NSE concentration, Inset indicates the corresponding calibration curve between recovered fluorescence and log NSE concentration in the range of 0.0001–1500 ng mL⁻¹ (c) Selectivity studies of proposed biosensor (d) Control experiment for the amino-GQDs/Ag@Ti₃C₂-MXene immunoelectrode.

(Fig. S12) based fluorescent immunosensing platforms toward different concentrations (0.0001–1500 ng mL⁻¹) of NSE. It has been found that the fluorescence intensity of protein functionalized amino-GQDs restore with increasing NSE antigen concentration. The restoration in the fluorescence intensity is linearly correlated to the added concentration and can be ascribed to the formation of the antigen-antibody immunocomplex (Chen et al., 2018; Das et al., 2018). For each added concentration, the formed complex increases the distance among donor-acceptor species. Consequently, there will be no energy transfer from the protein-functionalized amino-GQDs to the Ag@Ti₃C₂-MXene/Ti₃C₂-MXene, and hence the fluorescence intensity starts to restore gradually. Fig. 5b and Fig. S12d indicate the calibration plot between recovered fluorescence intensities and log NSE concentration for anti-NSE/amino-GQDs/Ag@Ti₃C₂-MXene and anti-NSE/amino-GQDs/Ti₃C₂-MXene, respectively. In case of anti-NSE/amino-GQDs/Ag@Ti₃C₂-MXene, an established linear correlation is obtained in the dynamic range of 0.0001–1500 ng mL⁻¹, described by the linear regression equation Eq. (2). Whereas, in case of anti-NSE/amino-GQDs/Ti₃C₂-MXene, a linear correlation is obtained in the range of 1–1000 ng mL⁻¹, described by Eq. (S2).

$$I = 771.54 \log_{10} \text{NSE (ng mL}^{-1}) + 3987.04, \text{ the Regression coefficient } R^2 = 0.99 \quad (2)$$

Further, the limit of detection (LOD) is calculated according to the standard equation (Eq. S3). The LOD for anti-NSE/amino-GQDs/Ag@Ti₃C₂-MXene and anti-NSE/amino-GQDs/Ti₃C₂-MXene immunoprobe is calculated as 0.05 pg mL⁻¹ and 0.34 ng mL⁻¹, respectively. Besides, we have compared the analytical performance of anti-NSE/amino-GQDs/Ag@Ti₃C₂-MXene fluorescent biosensor with classic 2D graphene (Fig. S13) and our previously reported AuNPs based sensing platforms. It is found that the anti-NSE/amino-GQDs/Ag@Ti₃C₂-MXene based biosensing platform exhibits better LOD, broader linear detection range, improved sensitivity, and a faster response time. Specifically, the sensitivity of Ag@Ti₃C₂-MXene based platform (~771 mL ng⁻¹) is exceeding two times in contrast to graphene (~352 mL ng⁻¹) as well as AuNPs (~333 mL ng⁻¹) (Kalkal et al., 2020) based platforms. Furthermore, the biosensing characteristics of the present fluorescent biosensor are summarized in Table 1, along with reported aptasensors, sandwich assays, and immunosensors for NSE detection.

Table 1

Analytical comparison of anti-NSE/amino-GQDs/Ag@Ti₃C₂-MXene based biosensor with earlier reported biosensing platforms for NSE detection.

Sr. No.	Analytical Platform	Technique	Linear range (ng mL ⁻¹)	Limit of detection	Sensitivity	Time (min)	Ref.
1.	NH ₂ -G/Thi/AuNPs POCT	Differential pulse Voltammetry (DPV)	1–500	10 pg mL ⁻¹	0.941 μA mL ng ⁻¹	18	Fan et al. (2017)
2.	MB-COOH/NH ₂ -Apt-5	Chemiluminescence (CL)	1–100	0.1 ng mL ⁻¹	26.34 mL ng ⁻¹	–	Zheng et al. (2019)
3.	Fc-g-Au@Pd-P(BBY) and rGO/Thi/AuPt NAs	Electrochemical Impedance spectroscopy (EIS)	0.0001–50.0	0.03 pg mL ⁻¹	–	–	Chen et al. (2020)
4.	anti-NSE/DA/TiO ₂ /FTO	Photocurrent	0.1–1000	0.05 ng mL ⁻¹	–	30	Li et al. (2017)
5.	CEA/anti-CEA/CNTs-AuNPs/GCE	Cyclic Voltammetry (CV)	0.10–200	0.04 ng mL ⁻¹	1.56 μA mL ng ⁻¹	20	Gao et al. (2011)
6.	FITC-anti-NSE/ALP-NSE/anti-FITC-MB	CL	0–300	0.2 ng mL ⁻¹	4774.8 mL ng ⁻¹	–	Fu et al. (2012)
7.	ITO/NiWO ₄ /Ab	Photocurrent	75–723	0.12 ng mL ⁻¹	–	–	Soomro et al. (2019)
8.	HRP-P4/anti-P4/GCE	chronoamperometry	0.50–12.5	0.20 ng mL ⁻¹	3.0 ± 0.1 nA ng ⁻¹ mL	15	Arévalo et al. (2010)
9.	anti-NSE/Au-Gra/NiHCFNPs/AuNCs/GCE	CV	0.001–100	0.3 pg mL ⁻¹	60.84 μA mL ng ⁻¹	30	Han et al. (2012)
10.	anti-NSE/amine-N-GQDs@AuNPs	Fluorescence Spectroscopy (FS)	0.0001–1000	0.09 pg mL ⁻¹	333.20 mL ng ⁻¹	16	Kalkal et al. (2020)
11.	anti-NSE/amino-GQDs/Ti ₃ C ₂ -MXene	FS	1–1000	0.34 ng mL ⁻¹	875.57 mL ng ⁻¹	–	This work
12.	anti-NSE/amino-GQDs/Ag@Ti ₃ C ₂ -MXene	FS	0.0001–1500	0.05 pg mL ⁻¹	771.54 mL ng ⁻¹	12	This work

3.5. Selectivity of the proposed fluorescent biosensor

The developed fluorescent biosensor has been found to exhibit good performance toward the detection of NSE biomarker. However, in human serum, various interfering biomarkers (other than NSE) such as cytokeratin-19 fragment (CYFRA-21-1), cardiac troponin-I (cTnI), endothelin-1 (ET-1), carcinoembryonic antigen (CEA) are also present. These interfering biomarkers may also contribute towards the fluorescence recovery of the fabricated biosensor. Therefore, it becomes crucial to examine the efficacy of developed biosensor in the presence of these potential serum biomarkers. In this context, Fig. 5c indicates the response of the biosensor in the presence of individual cancer biomarker (50 μL, 0.1 ng mL⁻¹) and mixture of all biomarkers. A marginal recovery in fluorescence has been observed with interfering cancer biomarkers. The fluorescence recovery difference is estimated to be less than 5% when compared to the blank sample (anti-NSE/amino-GQDs/Ag@Ti₃C₂-MXene). Additionally, the selectivity coefficient (SC) is also determined for each biomarker utilizing Eq. (S5) and found to be ~1. In addition, the corresponding analytical signal is recorded to examine the selectivity of the immunosensor in a mixture of NSE and other mentioned biomarkers, which commensurate with the analytical signal linked to NSE alone, as shown in Fig. 5c. These findings explicitly suggest that fluorescence recovery is caused by specific NSE biomarker, demonstrating the excellent selectivity of the proposed fluorescent biosensor for NSE detection.

3.6. Control and reproducibility studies

Under similar conditions, the fluorescence response of the amino-GQDs/Ag@Ti₃C₂-MXene has been recorded in the same range (0.0001–1500 ng mL⁻¹) as a controlled sample for NSE detection. The findings obtained (Fig. 5d) reveal that there is no substantial restoration of the fluorescence intensity against the added NSE concentration, suggesting that the restoration of fluorescence intensity is primarily due to the unique antibody-antigen interactions. Besides, fluorescent immunosensor reproducibility (Fig. S14) is determined by identifying NSE (50 μL, 1 ng mL⁻¹) using five distinctive fluorescent probes fabricated under comparable conditions. The measured relative standard deviation of less than 10 percent (% RSD) signifies higher reproducibility and good accuracy.

3.7. Real sample analysis

For real sample analysis, the collected serum samples are spiked with 50 μL of known NSE antigen concentrations (10, 20, 50, 100, and 150 ng mL^{-1}). Fig. S15a shows the results of the proposed immunosensor (anti-NSE/amino-GQDs/Ag@Ti₃C₂-MXene) toward five different NSE spiked serum samples. The incubation time of 12 min is provided for having the immunoreaction (antigen-antibody interactions) as in the previous experiment. For both the standard and spiked serum samples, a strong correlation suggesting a similar pattern of fluorescence intensity recovery has been obtained. The calibration plot between the fluorescence intensities and log of target biomarker concentration has been depicted in Fig. S15b. A linear relation has been realized, described by Eq. (S6). The % recovery in the spiked serum samples is determined using Eq. (3) and listed in Table S1.

$$\% \text{ recovery} = \frac{y_i - y_o}{y_s} \times 100 \quad (3)$$

Where y_s is the actual NSE spiked concentration and y_i , y_o are the obtained concentrations in spiked and unspiked samples, respectively. The anti-NSE/amino-GQDs/Ag@Ti₃C₂-MXene based fluorescent immunosensor exhibit an average recovery of ~98%. The obtained results signify that the fabricated immunosensor can quantitatively detect the NSE biomarker in the clinical samples.

4. Conclusions

In the present work, a potential fluorescent biosensor comprised of biofunctionalized graphene quantum dots and Ag@Ti₃C₂-MXene nanohybrid is developed for the quantitative NSE detection. The functionality of this selective, rapid, label-free, and highly sensitive biosensor relies on the fluorescence quenching of donor species (anti-NSE/amino-GQDs) by the acceptor species (Ag@Ti₃C₂-MXene), followed by the restoration of quenched fluorescence upon the addition of NSE antigen. The Ag@Ti₃C₂-MXene nanohybrid as dual-energy acceptor exhibits higher quenching efficiency (~94%) compared to bare Ti₃C₂-MXene (~87%), AgNPs (~84%) and earlier reported AuNPs (~81%). Simultaneously, the energy transfer efficiency improved to 70% compared to Ti₃C₂-MXene (54%), and AuNPs (43%). Moreover, the developed Ag@Ti₃C₂-MXene nanohybrid-based biosensor exhibit improved biosensing parameters such as broader linear detection range (0.0001–1500 ng mL^{-1}), better LOD (0.05 pg mL^{-1}), higher sensitivity (~771 mL ng^{-1}), and faster response time (12 min). It is worth mentioning that the sensitivity of Ag@Ti₃C₂-MXene based biosensing platform is exceeding two times in contrast to classic graphene (~352 mL ng^{-1}) and our earlier reported AuNPs (~333 mL ng^{-1}) based platforms. On the other hand, enhanced linear detection range and LOD are observed in contrast to bare Ti₃C₂-MXene and graphene. The present biosensor also reveals remarkable performance in serum samples with ~98% average spiked NSE restoration. In nutshell, the developed immunosensor exhibits remarkable biosensing characteristics that make it a promising platform for quantitative NSE detection. Further efforts should be made towards integrating this potential platform with microfluidics and flexible electronics in creating the miniaturized point-of-care device.

Declaration of competing interest

The authors declare that they have no known competing financial interests or personal relationships that could have appeared to influence the work reported in this paper.

Acknowledgments

The present work is supported by the Department of Biotechnology (No. BT/PR25095/NER/95/1011/2017) Government of India. A. Kalkal

and S. Kadian are grateful to the Ministry of Education, India for the fellowship and Microfluidic Devices & Heterogeneous Systems Lab, Centre for Nano Science and Engineering (CeNSE), IISc, Bengaluru, India for the Internship. P. Gopinath would like to thank the Department of Science and Technology (DST), Government of India, Technology Innovation Hub (TIH) [A Section-8 Company: Divyasampark]. Saurabh Kumar acknowledges the DST for the DST-INSPIRE Faculty Award (DST/INSPIRE/04/2017/002750). Authors are thankful to the Centre of Nanotechnology, Department of Biosciences and Bioengineering IIT Roorkee and CeNSE, IISc, Bengaluru, India, for providing the required infrastructure and various characterization facilities.

Appendix A. Supplementary data

Supplementary data to this article can be found online at <https://doi.org/10.1016/j.bios.2021.113620>.

Author contributions

Ashish Kalkal, Saurabh kumar and P. Gopinath conceptualized the work. P. Gopinath, Saurabh Kumar, Prosenjit Sen, and Sumit Kumar provided valuable inputs and edited the manuscript. Ti₃C₂-MXene, Ag@Ti₃C₂-MXene nanohybrid synthesis, and optimization were carried out at CeNSE, IISc Bengaluru. Ti₃C₂-MXene and Ag@Ti₃C₂-MXene nanohybrid characterizations, biosensor fabrication, optimization, analysis and manuscript writing were performed by Ashish Kalkal. Sachin Kadian and Gaurav Manik provided their input in the XRD, UV, XPS, and PL characterizations. Sumit Kumar provided his input in performing the lifetime spectra. All authors contributed to draft the manuscript.

References

- Amani, J., Maleki, M., Khoshroo, A., Sobhani-Nasab, A., Rahimi-Nasrabadi, M., 2018. An electrochemical immunosensor based on poly p-phenylenediamine and graphene nanocomposite for detection of neuron-specific enolase via electrochemically amplified detection. *Anal. Biochem.* 548, 53–59.
- Amjadi, M., Abolghasemi-Fakhri, Z., Hallaj, T., 2015. Carbon dots-silver nanoparticles fluorescence resonance energy transfer system as a novel turn-on fluorescent probe for selective determination of cysteine. *J. Photochem. Photobiol. Chem.* 309, 8–14.
- Anasori, B., Lukatskaya, M.R., Gogotsi, Y., 2017. 2D metal carbides and nitrides (MXenes) for energy storage. *Nature Reviews Materials* 2 (2), 16098.
- Arévalo, F.J., Messina, G.A., Molina, P.G., Zón, M.A., Raba, J., Fernández, H., 2010. Determination of progesterone (P4) from bovine serum samples using a microfluidic immunosensor system. *Talanta* 80 (5), 1986–1992.
- Atif, R., Inam, F., 2016. Reasons and remedies for the agglomeration of multilayered graphene and carbon nanotubes in polymers. *Beilstein J. Nanotechnol.* 7, 1174–1196.
- Bellunato, A., Arjmandi-Tash, H., Cesa, Y., Schneider, G.F., 2016. Chemistry at the Edge of Graphene 17 (6), 785–801.
- Bhatnagar, D., Kumar, V., Kumar, A., Kaur, I., 2016. Graphene quantum dots FRET based sensor for early detection of heart attack in human. *Biosens. Bioelectron.* 79, 495–499.
- Cha, J., Kyoung, W., Song, K., Park, S., Lim, T., Lee, J., Kang, H., 2016. Quantitative evaluation of the dispersion of graphene sheets with and without functional groups using molecular dynamics simulations. *Nanoscale research letters* 11 (1), 136–136.
- Chauhan, D., Pooja, Nirbhaya, V., Srivastava, C.M., Chandra, R., Kumar, S., 2020. Nanostructured transition metal chalcogenide embedded on reduced graphene oxide based highly efficient biosensor for cardiovascular disease detection. *Microchem. J.* 155, 104697.
- Chen, B., Su, Q., Kong, W., Wang, Y., Shi, P., Wang, F., 2018. Energy transfer-based biotransduction using optical nanomaterials. *J. Mater. Chem. B* 6 (19), 2924–2944.
- Chen, Y., Ge, X.-Y., Cen, S.-Y., Wang, A.-J., Luo, X., Feng, J.-J., 2020. Ultrasensitive dual-signal ratiometric electrochemical aptasensor for neuron-specific enolase based on Au nanoparticles@Pd nanoclusters-poly(bismarck brown Y) and dendritic AuPt nanoassemblies. *Sensor. Actuator. B Chem.* 311, 127931.
- Cui, S., Mao, S., Wen, Z., Chang, J., Zhang, Y., Chen, J., 2013. Controllable synthesis of silver nanoparticle-decorated reduced graphene oxide hybrids for ammonia detection. *Analyst* 138 (10), 2877–2882.
- Das, P., Sedighi, A., Krull, U.J., 2018. Cancer biomarker determination by resonance energy transfer using functional fluorescent nanoprobe. *Anal. Chim. Acta* 1041, 1–24.
- Fan, Y., Liu, J., Wang, Y., Luo, J., Xu, H., Xu, S., Cai, X., 2017. A wireless point-of-care testing system for the detection of neuron-specific enolase with microfluidic paper-based analytical devices. *Biosens. Bioelectron.* 95, 60–66.

- Fu, X., Meng, M., Zhang, Y., Yin, Y., Zhang, X., Xi, R., 2012. Chemiluminescence enzyme immunoassay using magnetic nanoparticles for detection of neuron specific enolase in human serum. *Anal. Chim. Acta* 722, 114–118.
- Gao, X., Zhang, Y., Wu, Q., Chen, H., Chen, Z., Lin, X., 2011. One step electrochemically deposited nanocomposite film of chitosan-carbon nanotubes-gold nanoparticles for carcinoembryonic antigen immunosensor application. *Talanta* 85 (4), 1980–1985.
- Ghidiu, M., Naguib, M., Shi, C., Mashtalir, O., Pan, L.M., Zhang, B., Yang, J., Gogotsi, Y., Billinge, S.J.L., Barsoum, M.W., 2014. Synthesis and characterization of two-dimensional Nb₄C₃ (MXene). *Chem. Commun.* 50 (67), 9517–9520.
- Ghosh, D., Chattopadhyay, N., 2015. Gold and silver nanoparticles based superquenching of fluorescence: a review. *J. Lumin.* 160, 223–232.
- Han, J., Zhuo, Y., Chai, Y.-Q., Yuan, Y.-L., Yuan, R., 2012. Novel electrochemical catalysis as signal amplified strategy for label-free detection of neuron-specific enolase. *Biosens. Bioelectron.* 31 (1), 399–405.
- Harding, M., McAllister, J., Hulks, G., Vernon, D., Monie, R., Paul, J., Kaye, S.B., 1990. Neuron specific enolase (NSE) in small cell lung cancer: a tumour marker of prognostic significance? *Br. J. Canc.* 61 (4), 605–607.
- He, X., Zhang, S., Pan, H., Chen, J., Xu, J., 2019. Horizontally aggregation of monolayer reduced graphene oxide under deep UV irradiation in solution. *Nanoscale Research Letters* 14 (1), 117.
- Huang, K., Li, Z., Lin, J., Han, G., Huang, P., 2018. Two-dimensional transition metal carbides and nitrides (MXenes) for biomedical applications. *Chem. Soc. Rev.* 47 (14), 5109–5124.
- Ikram, M., Raza, A., Imran, M., Ul-Hamid, A., Shahbaz, A., Ali, S., 2020. Hydrothermal synthesis of silver decorated reduced graphene oxide (rGO) nanoflakes with effective photocatalytic activity for wastewater treatment. *Nanoscale Research Letters* 15 (1), 95.
- Jackman, D.M., Johnson, B.E., 2005. Small-cell lung cancer. *Lancet* 366 (9494), 1385–1396.
- Kadian, S., Manik, G., Kalkal, A., Singh, M., Chauhan, R.P., 2019. Effect of sulfur doping on fluorescence and quantum yield of graphene quantum dots: an experimental and theoretical investigation. *Nanotechnology* 30 (43), 435704.
- Kalali, E.N., Guo, W., Wang, X., Xing, W., Song, L., Hu, Y., 2020. Effect of metal-based nanoparticles decorated graphene hybrids on flammability of epoxy nanocomposites. *Compos. Appl. Sci. Manuf.* 129, 105694.
- Kalkal, A., Allawadhi, P., Pradhan, R., Khurana, A., Bharani, K.K., Packirisamy, G., 2021a. Allium sativum derived carbon dots as a potential theranostic agent to combat the COVID-19 crisis. *Sensors International* 2, 100102.
- Kalkal, A., Kadian, S., Pradhan, R., Manik, G., Packirisamy, G., 2021b. Recent advances in graphene quantum dot-based optical and electrochemical (bio)analytical sensors. *Materials Advances* 2 (17), 5513–5541.
- Kalkal, A., Kumar, S., Kumar, P., Pradhan, R., Willander, M., Packirisamy, G., Kumar, S., Malhotra, B.D., 2021c. Recent advances in 3D printing technologies for wearable (bio)sensors. *Additive Manufacturing* 46, 102088.
- Kalkal, A., Pradhan, R., Kadian, S., Manik, G., Packirisamy, G., 2020. Biofunctionalized graphene quantum dots based fluorescence biosensor toward efficient detection of small cell lung cancer. *ACS Applied Bio Materials* 3 (8), 4922–4932.
- Khazaei, M., Arai, M., Sasaki, T., Chung, C.-Y., Venkataramanan, N.S., Estili, M., Sakka, Y., Kawazoe, Y., 2013. Novel electronic and magnetic properties of two-dimensional transition metal carbides and nitrides. *Adv. Funct. Mater.* 23 (17), 2185–2192.
- Kumar, S., Ashish, Kumar, S., Augustine, S., Yadav, S., Yadav, B.K., Chauhan, R.P., Dewan, A.K., Malhotra, B.D., 2018a. Effect of Brownian motion on reduced agglomeration of nanostructured metal oxide towards development of efficient cancer biosensor. *Biosens. Bioelectron.* 102, 247–255.
- Kumar, S., Kalkal, A., 2021. 3 - electrochemical detection: cyclic voltammetry/differential pulse voltammetry/impedance spectroscopy. In: Khondakar, K.R., Kaushik, A.K. (Eds.), *Nanotechnology in Cancer Management*. Elsevier, pp. 43–71.
- Kumar, S., Kumar, J., Narayan Sharma, S., Srivastava, S., 2019a. rGO integrated MEHPV and P3HT polymer blends for bulk hetero junction solar cells: a comparative insight. *Optik* 178, 411–421.
- Kumar, Sumit, Sharma, Shailesh N., Kumar, Jitendra, 2019b. Comparative charge transport study of MEHPV-TiO₂ and P3HT-TiO₂ nanocomposites for hybrid bulk heterojunction solar cells. *J. Nanosci. Nanotechnol.* 6, 3408–3419. <https://doi.org/10.1166/jnn.2019.16130>.
- Kumar, S., Kumar, J., Sharma, S.N., 2020. Investigation of charge transfer properties in MEHPV and rGO-AA nanocomposites for Green organic photovoltaic application. *Optik* 208, 164540.
- Kumar, S., Lei, Y., Alshareef, N.H., Quevedo-Lopez, M.A., Salama, K.N., 2018b. Biofunctionalized two-dimensional Ti₃C₂ MXenes for ultrasensitive detection of cancer biomarker. *Biosens. Bioelectron.* 121, 243–249.
- Kumar, S., Sharma, J.G., Maji, S., Malhotra, B.D., 2016. Nanostructured zirconia decorated reduced graphene oxide based efficient biosensing platform for non-invasive oral cancer detection. *Biosens. Bioelectron.* 78, 497–504.
- Li, H., Xiao, Q., Lv, J., Lei, Q., Huang, Y., 2017. Dopamine modified hyperbranched TiO₂ arrays based ultrasensitive photoelectrochemical immunosensor for detecting neuron specific enolase. *Anal. Biochem.* 531, 48–55.
- Liu, G., Zou, J., Tang, Q., Yang, X., Zhang, Y., Zhang, Q., Huang, W., Chen, P., Shao, J., Dong, X., 2017. Surface modified Ti₃C₂ MXene nanosheets for tumor targeting photothermal/photodynamic/chemo synergistic therapy. *ACS Appl. Mater. Interfaces* 9 (46), 40077–40086.
- Mahdavi, M., Sharifpur, M., Ahmadi, M.H., Meyer, J.P., 2019. Aggregation study of Brownian nanoparticles in convective phenomena. *J. Therm. Anal. Calorim.* 135 (1), 111–121.
- Naguib, M., Kurtoglu, M., Presser, V., Lu, J., Niu, J., Heon, M., Hultman, L., Gogotsi, Y., Barsoum, M.W., 2011. Two-dimensional nanocrystals produced by exfoliation of Ti₃AlC₂. *Adv. Mater.* 23 (37), 4248–4253.
- Neema, P.M., Tomy, A.M., Cyriac, J., 2020. Chemical sensor platforms based on fluorescence resonance energy transfer (FRET) and 2D materials. *Trac. Trends Anal. Chem.* 124, 115797.
- Pandey, R.P., Rasool, K., Madhavan, V.E., Aissa, B., Gogotsi, Y., Mahmoud, K.A., 2018. Ultrahigh-flux and fouling-resistant membranes based on layered silver/MXene (Ti₃C₂Tx) nanosheets. *J. Mater. Chem.* 6 (8), 3522–3533.
- Peng, C., Yang, X., Li, Y., Yu, H., Wang, H., Peng, F., 2016. Hybrids of two-dimensional Ti₃C₂ and TiO₂ exposing {001} facets toward enhanced photocatalytic activity. *ACS Appl. Mater. Interfaces* 8 (9), 6051–6060.
- Peng, X., Zhang, Y., Lu, D., Guo, Y., Guo, S., 2019. Ultrathin Ti₃C₂ nanosheets based “off-on” fluorescent nanoprobe for rapid and sensitive detection of HPV infection. *Sensor. Actuator. B Chem.* 286, 222–229.
- Pradhan, R., Kalkal, A., Jindal, S., Packirisamy, G., Manhas, S., 2021a. Four electrode-based impedimetric biosensors for evaluating cytotoxicity of tamoxifen on cervical cancer cells. *RSC Adv.* 11 (2), 798–806.
- Pradhan, R., Raisa, S.A., Kumar, P., Kalkal, A., Kumar, N., Packirisamy, G., Manhas, S., 2021b. Optimization, fabrication, and characterization of four electrode-based sensors for blood impedance measurement. *Biomed. Microdevices* 23 (1), 9.
- Rudin, C.M., Brambilla, E., Faivre-Finn, C., Sage, J., 2021. Small-cell lung cancer. *Nature Reviews Disease Primers* 7 (1), 3.
- Shao, K., Wang, L., Wen, Y., Wang, T., Teng, Y., Shen, Z., Pan, Z., 2019. Near-infrared carbon dots-based fluorescence turn on aptasensor for determination of carcinoembryonic antigen in pleural effusion. *Anal. Chim. Acta* 1068, 52–59.
- Shi, J., Tian, F., Lyu, J., Yang, M., 2015. Nanoparticle based fluorescence resonance energy transfer (FRET) for biosensing applications. *J. Mater. Chem. B* 3 (35), 6989–7005.
- Shi, Y.-e., Han, F., Xie, L., Zhang, C., Li, T., Wang, H., Lai, W.-F., Luo, S., Wei, W., Wang, Z., Huang, Y., 2019. A MXene of type Ti₃C₂Tx functionalized with copper nanoclusters for the fluorometric determination of glutathione. *Microchimica Acta* 187 (1), 38.
- Shibayama, T., Ueoka, H., Nishii, K., Kiura, K., Tabata, M., Miyatake, K., Kitajima, T., Harada, M., 2001. Complementary roles of pro-gastrin-releasing peptide (ProGRP) and neuron specific enolase (NSE) in diagnosis and prognosis of small-cell lung cancer (SCLC). *Lung Canc.* 32 (1), 61–69.
- Song, Q., Ye, F., Kong, L., Shen, Q., Han, L., Feng, L., Yu, G., Pan, Y., Li, H., 2020. Graphene and MXene nanomaterials. Toward High-Performance Electromagnetic Wave Absorption in Gigahertz Band Range 30 (31), 2000475.
- Soomro, R.A., Jawaid, S., Zhu, Q., Abbas, Z., Xu, B., 2020. A mini-review on MXenes as versatile substrate for advanced sensors. *Chin. Chem. Lett.* 31 (4), 922–930.
- Soomro, R.A., Kalwar, N.H., Avci, A., Pehlivan, E., Hallam, K.R., Willander, M., 2019. In-situ growth of NiWO₄ saw-blade-like nanostructures and their application in photoelectrochemical (PEC) immunosensor system designed for the detection of neuron-specific enolase. *Biosens. Bioelectron.* 141, 111331.
- Su, H., Zhang, C., Li, X., Wu, L., Chen, Y., 2018. Aggregation prevention: reduction of graphene oxide in mixed medium of alkylphenol polyoxyethylene (7) ether and 2-methoxyethanol. *RSC Adv.* 8 (68), 39140–39148.
- Sun, Y., Chen, D., Liang, Z., 2017. Two-dimensional MXenes for energy storage and conversion applications. *Materials Today Energy* 5, 22–36.
- Swaminathan, H., Ramar, V., Balasubramanian, K., 2017. Excited-state electron and energy transfer dynamics between 2D MoS₂ and GO/RGO for turn ON BSA/HSA sensing. *J. Phys. Chem. C* 121 (23), 12585–12592.
- Tian, F., Lyu, J., Shi, J., Yang, M., 2017. Graphene and graphene-like two-denominational materials based fluorescence resonance energy transfer (FRET) assays for biological applications. *Biosens. Bioelectron.* 89, 123–135.
- Tilaki, R.M., Irajizad, A., Mahdavi, S.M., 2006. Stability, size and optical properties of silver nanoparticles prepared by laser ablation in different carrier media. *Appl. Phys.* 84 (1), 215–219.
- Torres-Mendieta, R., Ventura-Espinosa, D., Sabater, S., Lancis, J., Mínguez-Vega, G., Mata, J.A., 2016. In situ decoration of graphene sheets with gold nanoparticles synthesized by pulsed laser ablation in liquids. *Sci. Rep.* 6 (1), 30478.
- Vedala, H., Sorescu, D.C., Kotchey, G.P., Star, A., 2011. Chemical sensitivity of graphene edges decorated with metal nanoparticles. *Nano Lett.* 11 (6), 2342–2347.
- Xiao, K., Wang, K., Qin, W., Hou, Y., Lu, W., Xu, H., Wo, Y., Cui, D., 2017. Use of quantum dot beads-labeled monoclonal antibody to improve the sensitivity of a quantitative and simultaneous immunochromatographic assay for neuron specific enolase and carcinoembryonic antigen. *Talanta* 164, 463–469.
- Zhang, Q., Wang, F., Zhang, H., Zhang, Y., Liu, M., Liu, Y., 2018. Universal Ti₃C₂ MXenes based self-standard ratiometric fluorescence resonance energy transfer platform for highly sensitive detection of exosomes. *Anal. Chem.* 90 (21), 12737–12744.
- Zheng, Y., Zhao, Y., Di, Y., He, L., Liao, S., Li, D., Liu, X., 2019. In vitro selection of DNA aptamers for the development of chemiluminescence aptasensor for neuron-specific enolase (NSE) detection. *RSC Adv.* 9 (27), 15513–15520.
- Zhou, H., Wu, F., Fang, L., Hu, J., Luo, H., Guan, T., Hu, B., Zhou, M., 2020. Layered NiFe-LDH/MXene nanocomposite electrode for high-performance supercapacitor. *Int. J. Hydrogen Energy* 45 (23), 13080–13089.
- Zhu, X., Pang, X., Zhang, Y., Yao, S., 2019. Titanium carbide MXenes combined with red-emitting carbon dots as a unique turn-on fluorescent nanosensor for label-free determination of glucose. *J. Mater. Chem. B* 7 (48), 7729–7735.
- Zou, G., Zhang, Z., Guo, J., Liu, B., Zhang, Q., Fernandez, C., Peng, Q., 2016. Synthesis of MXene/Ag composites for extraordinary long cycle lifetime lithium storage at high rates. *ACS Appl. Mater. Interfaces* 8 (34), 22280–22286.